OE Optical Engineering

REVIEW

Analysis of structures and technologies of various types of photodetectors used in laser warning systems: a review

Shahram Mohammadnejad* and **Meysam Aasi**
Iran University of Science and Technology, School of Electrical Engineering, Nanoptronics Research Center, Tehran, Iran

ABSTRACT. With the advancement of laser technology in recent decades, this device has been used in a wide range of applications, such as medical sciences, military, industry, holography, spectroscopy, and astronomy. In past years, military operations for better communication depended on radiofrequency. Vulnerability to security threats and exposure to electromagnetic interference were the main problems of this electromagnetic spectrum region. Therefore, attention was drawn to the visible and infrared (IR) regions. This spectrum provided a secure transfer of the data. The probability of intercepting a laser signal is very low due to the divergence of the narrow beam and the coherence of its optical beam. Hence, it has made this device a good candidate for secure military operations. As a result, the laser based-devices and laser-guided weapons (LGW), such as laser target designator and beam riders, have become an undeniable tool on battlefields. Reduction of the vulnerability to the LGW threats by providing laser detection, angle of arrival, wavelength discrimination, and temporal characterization is the main intention of the laser warning system (LWS). This system consists of three major subsystems. The optical subsystem will consist of spectral filters, focusing lenses, and the detection one, which is made of a few detectors in a unique array's configuration [especially IR photodetector (IRPD)], and the processing subsystem. In the last decades, with the progress made in nanofabrication and nanotechnology, consequential research has been done to enhance the performance of IRPDs, such as increasing the production yield, making it simple in the fabrication processes, lowering the fabrication cost, and increasing the operating temperature. This review paper gives a particular concentration to the photodetectors used in the detection subsystem of LWSs. In addition, some nanostructures have been surveyed to enhance the optical coupling and light–matter interaction of IRPD. Also, all studied structures are compared in a table. Finally, the detection subsystem we simulated and built at the Nanoptronics Research Center will be analyzed.

 [DOI: 10.1117/1.OE.62.9.090901]

Keywords: laser; laser warning system; infrared photodetector; nanostructure; optical coupling

Paper 20230430V received May 17, 2023; revised Aug. 10, 2023; accepted Aug. 16, 2023; published Sep. 12, 2023.

1 Introduction

The most important applications of lasers are in health sciences, engineering, security, and military systems. An increase in the maturity of compact optical and laser devices has improved their abilities for military purposes. Therefore, today's modern battlefield consists of many laser

*Address all correspondence to Shahram Mohammadnejad, shahramm@iust.ac.ir

Table 1 Projects for demonstrating laser technology in military operations.

Program title	Comments	Year
Boeing high-energy laser mobile demonstrator	To track and destroy aerial targets from ground-based vehicles using 10 kW solid state laser at IR wavelength[4]	2011 to ongoing
Robust electric laser initiative	A joint project operated by the department of defense, Lockheed Martin, Northrop Grumman, and Boeing for producing 100 kW laser[5]	2013 to ongoing
Solid-state laser technology maturation program	Operated by the office of Navy Research, whose aim is to provide mature HEL weapons[6]	2012 to ongoing
Aero-adaptive/aero-optic beam control program	This is a joint program of DARPA and AFRL whose objective is to deploy HELs on arm aircraft that are able to fire in any direction[7]	2013 to ongoing

weapon systems: laser-assisted weapons, which are missiles or projectiles deployed to a target via a laser beam, laser rangefinders (LRFs) for detecting the distance and direction of a potential target,[1] and directed energy (DE) weapons, which have the potential to leave devastating effects on a large area.[2] One of the advantages of using lasers in these systems is the transmission at the speed of light, which allows laser-dependent weapons to be engaged immediately after target detection. Besides, the DE of the laser provides less collateral damage and can operate in secret.[3]

Table 1 shows some of the ongoing military laser projects.

Kaushal and Kaddom[8] scrutinized the use of lasers in military tactical operations.

Reliable laser source detection can minimize these damages and provide accurate information to take action.[9]

The principle of laser threat performance is using a laser beam to increase the chance of a weapon hitting the target. To this end, these threats fall into four classes:

- LRF: The most rampant laser system will typically be designed as a single pulse to transmit the laser beam and estimate its distance to the target using its reflection. Laser transmitters generating radiation at 905, 1064, and 1510 to 1550 nm are often used in rangefinders.
- Laser target designator: The most standard invention in today's world of war instruments. This system has multiple pulses and can be encoded more accurately with the corresponding weapon.
- The designators use lasers generating radiation at a wavelength of 1064 and about 1500 nm.
- Laser beam rider (LBR): The most lethal laser threat that the laser uses to steer a missile or projectile onto a target. It uses continuous wave (CW) or pulse wave configuration. The most important difference from this type of threat is that the laser energy will not focus on the target but on the missile's tail end. Furthermore, low signal strength will make detecting this type of system complexity.
- Mainly wavelengths of 905 nm and 1.064 μm are used in LBRs. The Russian-built AT-14 Kornet Anti-Tank Guided Missile is an example of this type of system.[10]
- DE weapon: DE threats include weapons that use DE to destroy and disable enemy targets. Radiofrequency (RF) weapons, lasers, active denial technology, DE anti-satellite, and high-power microwave weapon systems are examples of this threat.[11]

As discussed above, a laser threat from an enemy can come across any instance from any direction and will remain detectable for only 5 to 10 ns.[12] Hence, defense forces provide rapid threat detection and proper response to prevent damage using laser warning system (LWS). This system consists of optical, detection, and processing subsystems and usually displays several parameters of incident radiation, such as the angle of arrival (AoA), wavelength, and power. It must detect and store all the information regarding the laser threat within this minor interval. Many research centers and defense agencies worldwide are developing this system to protect

military platforms from laser weapons. Our group in the Nanoptronics Research Center (NRC) at Iran University of Science and Technology (IUST) proposed a new optical subsystem for optimizing the optical array using six lenses for gathering the incident radiation.[13]

The most commonly used lasers in today's modern battlefield are in the infrared (IR) region, especially near-infrared (NIR). Lasers such as Nd: YAG with a wavelength of 1064 nm, Er: YAG laser, and a Raman shifted Nd: YAG laser with a 1530 to 1550 nm wavelength. Also, ruby laser at 694 nm and carbon dioxide (CO_2) lasers with a wavelength of 10.6 μm was reported.[14]

Detectors used in LWS are usually based on a semiconductor photodetector (PD) array, typically cryogenically or thermal-electric cooled. Sometimes avalanche photodiodes (APD), photoconductivity (PC), photoelectromagnetic (PEM), or photodiffusion (Dember effect) devices are often use without cooling.[15] APDs have been widely used in systems with high-frequency applications and high-speed detection. With the advancement of quantum telecommunications, three-dimension (3D) radar imaging, weak signal detection, and modern military applications, the need for low-noise and high-sensitivity PDs has become more pronounced. Therefore, Si and AlGaAs-based APDs have been widely used in technical fields, especially in NIR and visible detection systems. Si APDs cover the spectral range of 400 to 1100 nm, and the InGaAs APDs cover 950 to 1550 nm. An APD provides higher sensitivity than a standard photodiode and is for extreme low-level light (LLL) detection and photon counting.[16] Yttrium aluminum garnet (YAG) series detectors are optimized for fast response at 1060 nm, YAG laser light wavelength, and low capacitance for high operating speed and low noise. These detectors are suitable for sensing low-intensity light reflected from laser beams from objects (in ranging applications). The SPOT series of quadrant detectors will be used in targeting applications. These are all n on P devices. These detectors will require reverse bias voltage and work in the PC mode for high-speed applications.[17]

Today, AlGaAS and HgCdTe-based PDs are suitable for detecting short-wavelength infrared (SWIR $\approx$ 1 to 3 μm). Besides the standard InGaAs detectors with a cut-off wavelength of 1.67 μm, extended-wavelength (EW) InGaAs detectors have been in high demand in gas sensing, spectroscopy, and food safety. These detectors have been researched and developed for three decades. One of these critical and leading sources of these detectors in the market of aerospace and defense applications in the manufacture and commercialization is Teledyne Judson Technologies. These products are the essential discrete detectors with a cut-off wavelength of 1.9 to 2.6 μm with a P on n planar structures and in either single elements or linear arrays capable of operating from room temperature to thermoelectrically cooled temperatures.[18]

One of the detection structures that has attracted a lot of attention due to the simultaneous advantage of operating at room temperature and fast response time is IR PEM detectors. A variable gap semiconductor, mercury–cadmium–zinc–telluride (Hg-Cd-Zn-Te), with graded composition and doping level profiles helps the manufacturer to achieve the highest possible sensitivity with its IR PEM detectors and adjust the absorption wavelength in a wide range of the IR spectrum (2 to 12 μm). Other advantages of this type of PD include no need for bias, sub-nanosecond response time, lightweight, rugged, and reliability, which makes it a good choice for use in LWSs.[19]

Four-quadrant detectors (4-QD) are another suitable device with advantages, such as high light-sensitive areas, fast response, and low noise. The LWS based on this detection structure is highly accurate. Still, its circuit structure is very complex, and obtaining the source of the threat is dependent on the processing algorithm.[20–22]

The new class of LWS will also use a multi-wavelength detector. This type of detector has several semiconductor layers subdivided into multi-dielectric screens and focus the laser light into one of the semiconductors (proportional to the wavelength).[23] An active pixel-imaging sensor, integrated readout circuit, and array of detectors could be used in LWS.

Various techniques have been used to detect the position of the incoming laser designator, with varying accuracy levels, from soldier-mounted course detection to multiple discrete detectors positioned strategically on artillery equipment, evolving ultimately to devices, such as Excelitas Technologies' high angular resolution laser irradiance detector (HARLID). The HARLID combines, within a single TO-8 can, multi-element silicon and InGaAs detector array and encoding mechanism to help to determine the incident angle. Using two detectors enables the

detection of the most commonly deployed laser designator wavelengths, from 500 to 1650 nm, on the battlefield.[24] We will not focus on incident angle detection methods because it is beyond the scope of this article, but you can refer to Refs. 25–27 for further studies. One of the most critical parameters in LWSs is the false alarm rate (FAR). The LWS must be able to detect the real laser threat radiation and not interfere with the background radiations and noises. To avoid this problem, the use of methods, such as optical interferometers[28,29] and photoacoustic design,[30] is suggested.

In this paper, we first provide a basic configuration of LWS and examine a model that considers all the influential aspects of laser threat beam to the detection subsystem of LWS. Then, we stated the general theory and evaluation parameters of PDs. Then, we went to the article's main body, analyzing the sensors used in this system. Finally, in a table, we excavate and compare several previously built plans. It should be noted that the design of a TIA circuit with two stages of voltage amplifier to condition a current of 1 μA from the output of the PD was simulated and built in the NRC of the Iran University of Science and Technology.

2 Basic Configuration of LWS and Characteristics

The warning laser beam will diverge in the beam and weaken its original power when passing through the atmosphere and facing atmospheric disturbances. This divergence is an entirely destructive process, making it difficult for the detection subsystem to receive the signal. Therefore, optical signal focusing elements such as focusing lenses are this subsystem's most crucial element. One of the filtration or threat identification mechanisms is also necessary. It may be an adjustable threshold mechanism, which filters receive noise signals by dynamically adjusting a noise threshold level based on detected ambient light conditions. A correlation filtering mechanism filters received noise signals based on correlation criteria of the timing of received laser radiation by spatially separated laser detectors—the friendly fire elimination mechanism filters detected laser radiation transmitted by a non-threat source. The threat identification mechanism may also be a time mapping mechanism that identifies and characterizes the threat based on pulse mappings of the received laser radiation or a first arrival mechanism that determines the threat direction based on where the received laser radiation arrived first from among multiple laser detectors.[1]

After focusing and filtering, the laser beam will enter the detection subsystem to convert the existing optical signal into an electrical signal. Then, the signal will process by the digital signal processor system. In this subsystem, the laser beam's characterizations, such as laser detection, AoA, wavelength discrimination, and temporal characterization, have been obtained to perform specific countermeasures (Fig. 1).[31]

Figure 2 shows an LWS model that can simulate all aspects of the LBR threat and the laser warning receiver (LWR) scenario. It simulates components of the factors affecting the propagation of laser beams in the atmosphere until they reach the target.

Figure 3 shows the performance of noise filtering, the mechanisms of threat beam detection from non-threat, and its characterization.

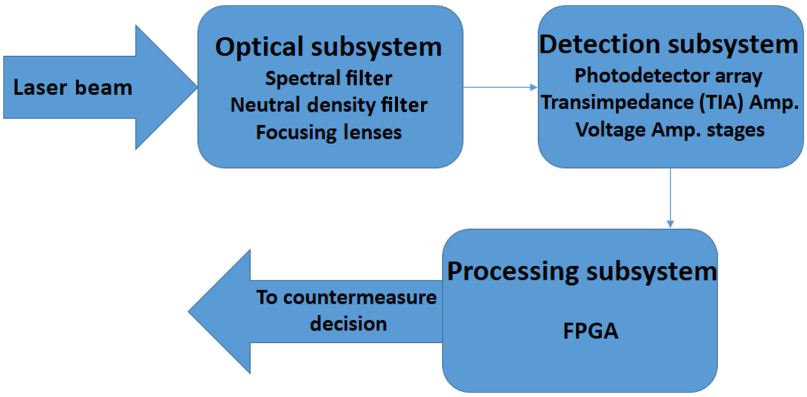

Fig. 1 LWS blocks.[13]

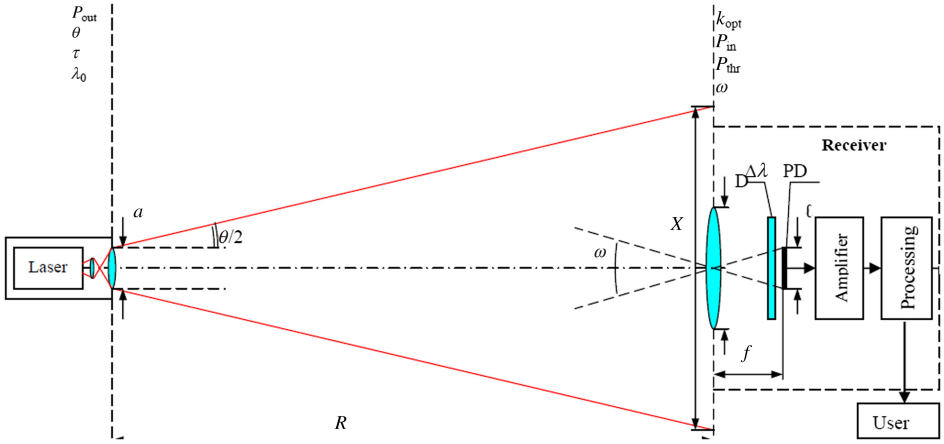

Fig. 2 Configuration of LWS.[32] P_{out}, laser irradiator output power; τ_l, pulse length; θ, laser irradiator divergence angle; λ_0, radiation wavelength; a, transmitter aperture diameter; R, distance from transmitter to receiver; P_{in}, laser radiation power at the receiver input; x, the size of the laser beam on the target receiver; D, receive aperture diameter; l, size of PD sensor area; f, focal length of receiving the target; ω, receiver FOV; P_{thr}, threshold power; k_{opt}, loss coefficient in optical elements; T_{abs}, attenuation of atmospheric absorption; T_{sct}: attenuation of atmospheric scattering; Δf, bandwidth; T, temperatures; $\Delta\lambda$, medium bandwidth filter.

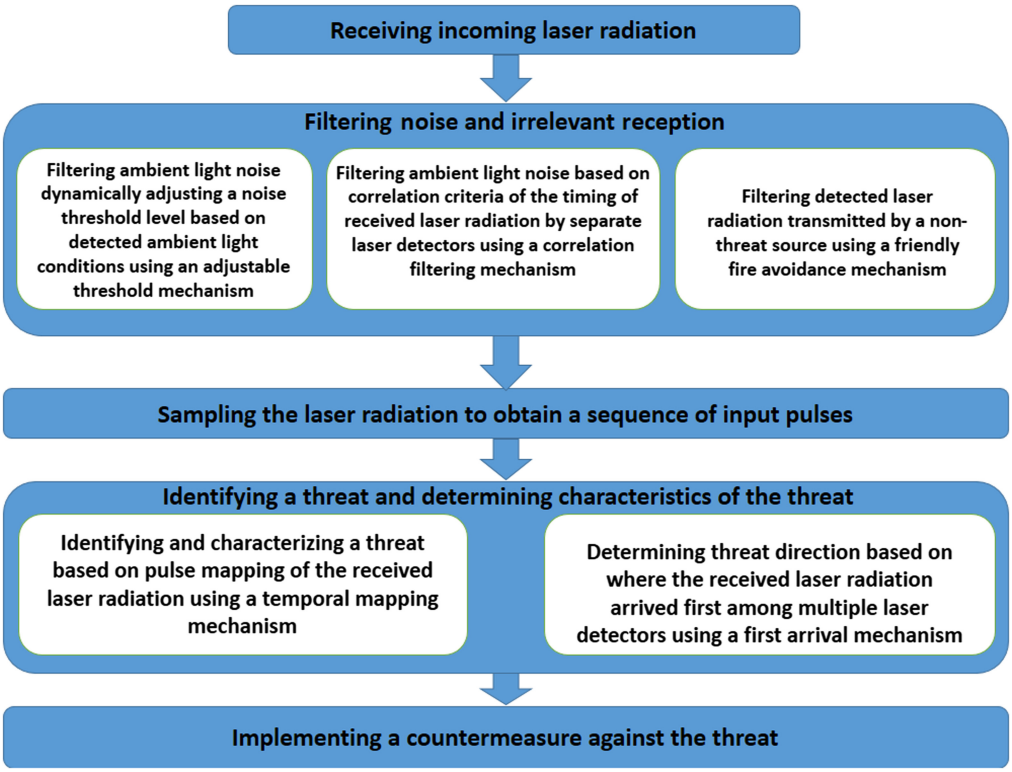

Fig. 3 Flow diagram of LWS performance.[1]

To evaluate the performance of an LWS, the following parameters are critical:

2.1 Probability of Detection

The function of system parameters such as source signal level, angular position in detector field of view (FOV), weather conditions, noise level, sun position in system FOV, and working range. The most convenient definition of POD is the number of diagnostic pulses divided by the number of transmissions. The mathematical approximation is obtained from the following equation:

$$P_d = \frac{1}{2}\left(1 + \operatorname{erf}\frac{I_s - I_T}{\sqrt{2I_N}}\right). \quad (1)$$

In this regard, erf is the standard error function, I_s, I_T, and I_N represent the level of signal, threshold, and noise, respectively.

2.2 False Alarm Rate

Lack of correct detection of the system in detecting laser threats. Unique algorithms (which can be added to the hardware and software of LWS) are used to reduce the FAR. For example, to reduce the background radiation, they reduce the FOV. However, in this case, we will need several detection channels. Also, several false alarms from other sources with time profiles are similar to laser threat sources. Among the conventional sources, we can mention solar radiation and lightning.

2.3 Dynamic Range

The problem is caused by the fact that when the electronic part works in linear mode, it cannot operate in a wide dynamic range before saturation and pulse broadening occur. Finally, if the system is not appropriately designed, some or all front-end electronics will be destroyed under high-frequency signals. To solve this problem, logarithmic amplifiers and current limiting circuits are used in LWRs.

2.4 Angular Resolution

Angular resolution is required for positioning laser sources depending on the level of access to countermeasures and their type. There are several ways to achieve this clarity. One of the exciting methods focuses on detectors. For example, they use several single detectors or an array of them. In this case, we face a basic problem, which is a sudden increase in the number of detection channels. Also, imaging sensors, optical fiber handles, and mask encryption tools have been successfully used. Finally, size and price factors are very critical in design.

2.5 Noise Level

The sensitivity limitation in LWS is usually due to background radiation in daylight. Threshold sensitivity is usually obtained using the worst conditions when the sun is in the FOV.

The exact calculations of these parameters are out of the main discussion of this article, so we only introduce the necessary sources for further study.[33–37]

3 General Theory of Photodetector

A PD is a critical device in the front end of an optical receiver that converts the incoming optical signal into an electrical signal. Semiconductor PDs are the main types of PDs used in optical communication systems because of their small size, fast detection speed, and high detection efficiency. It is a thick flat piece of homogeneous semiconductor with a factual electrical area A_e and can be coupled to IR radiation by the optical region A_o. Optical concentrators increase the rate A_o/A_e (Fig. 4).

Since being developed in the 1960s, it has been used in imaging, sensing, and communication applications.[38]

To select a suitable PD in an LWS, characterizations such as responsivity (A/W), spectral response range and peak (nm), photosensitivity (A/W), detectivity $(\text{cm.Hz}^{1/2}/\text{W})$, response time (ns), dark current (nA), bandwidth (MHz), effective photosensitive size (mm), quantum efficiency (%), reverse breakdown voltage (V), terminal capacity (pF), excess noise index, breakdown voltage temperature coefficient (V/°C), operating temperature range (°C) and, the noise equivalent power (NEP) $(\text{W}/\text{Hz}^{1/2})$ must be considered.

Responsivity (R) is an essential characteristic in PDs that quantum efficiency and photoelectric gain play a key role in determining. The photoelectric gain (g) is the number of carriers passing through the contact per generated pair, and it is defined simply as the ratio of photoelectron lifetime to transit time. This characteristic indicates how the electron–hole pairs can generate a response current in PDs.

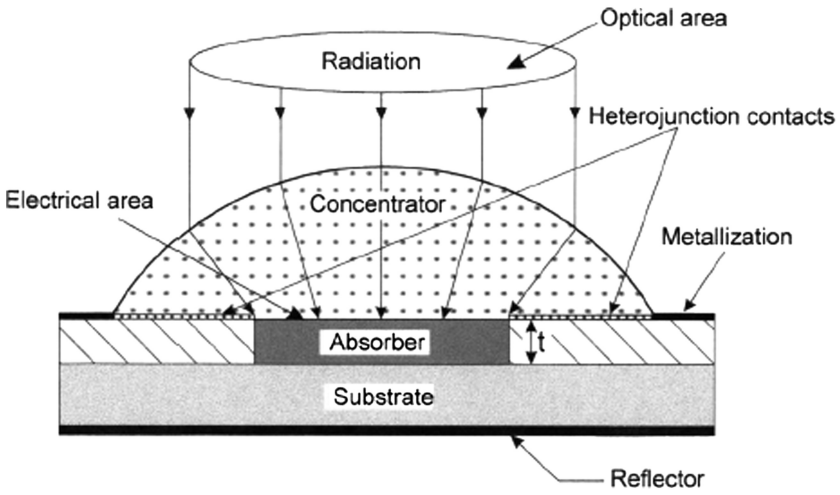

Fig. 4 Schematic illustration of a general PD.[39]

The spectral response of a PD is the range of optical wavelengths or frequencies in which the detector has a significant responsivity. The spectral response obtained from Eq. (2):

$$R_i = \frac{\lambda\eta}{hc} qg, \tag{2}$$

where λ is the wavelength, h is the Planck's constant, c is the light velocity, and q is the electron charge.

Photosensitivity (S) quantifies the minimum amount of light needed to produce an electronic signal and is typically wavelength-dependent.

Detectivity (D^*) of a PD is a figure of merit, defined as the inverse of the NEP. The larger the detectivity of a PD, the more it is suitable for detecting weak signals, which compete with the detector noise. It defines by Eq. (3):

$$D^* = \frac{R_i(A_0\Delta f)^{1/2}}{I_n}. \tag{3}$$

Assuming that the noise current and the current gain for the photocurrent are equal, the noise current generated by the generation and recombination processes is obtained from Eq. (4):

$$I_n^2 = 2(G+R)A_e t\Delta f q^2 g^2, \tag{4}$$

where G and R are the generations and recombination rates, Δf is the frequency band, and t is the thickness of the detector. According to the equation, 2-4 D^* can be expressed as Eq. (5):

$$D^* = \frac{\lambda}{hc}\left(\frac{A_o}{A_e}\right)^{1/2}\eta[2(G+R)t]^{-1/2}. \tag{5}$$

For a given wavelength and temperature, the highest performance can be achieved when $\eta/[(G+R)t]^{1/2}$ has its maximum value, which corresponds to the highest ratio of the sheet optical generation to the square root of sheet thermal generation and recombination. This means that quantum efficiency must be achieved in a thin device. The performance may be increased for a given wavelength and operating temperature by reducing the number of generation and recombination acts $(G+R)\times(A_e t)$.

Response time (t_r, t_f) of PD is when it takes the detector output to change in response to changes in the input light intensity. It depends mainly on the transit time of the photocarriers in the depletion region, the diffusion time of photocarriers outside the depletion region, and the circuit's RC time constant.

Dark current (I_d) is the current from a PD, which occurs even without light input. It includes the photocurrent produced by the background radiation and the saturated current of the PDs.

Bandwidth (BW) is the difference between the high and low cut-off frequencies measured in Hertz. The bandwidth of the PD is approximately related to the rise time $(0.35/t_r)$.

The effective photosensitive area corresponds to the size of the actual light-sensitive region, independent of the package size.

Quantum efficiency (η) usually indicates how a detector can couple with electromagnetic radiation and will be defined as the number of electron–hole pairs generated per incident photon.

Reverse breakdown voltage (V_{BR}) is the level of reverse voltage cause the breakdown and deterioration of the detector.

The terminal capacity (C_t) is the capacitance between the cathode and anode terminal of PD.

The excess noise factor (x) is a function of the carrier ionization ratio, k, where k is usually defined as the ratio of the hole to electron ionization probabilities ($k < 1$).

V_{BR} temperature coefficient (Γ) describes the relative change of a physical property associated with a given change in temperature.

The operating temperature (T) is the ambient temperature range in a PD operation.

NEP is the amount of incident photon energy equivalent to the intrinsic noise level of the device, providing a signal-to-noise ratio (SNR) of one $\left(\frac{\text{noise current}(\text{A}/\sqrt{\text{Hz}})}{\text{responsivity at }\lambda_p(\text{A/W})}\right)$.

An optimized detector should include the following:

I. The active region (base) with slight doping performs as an IR beam absorber. Its band gaps, geometric shapes, and doping must be carefully selected. The active area surface must be separated from the ambient by a material that does not produce carriers. Besides, the carriers built in the absorber by light should stay away from surfaces where quantum efficiency will reduce due to recombination.
II. Electrical connections to the light-sensitive base region will generate charge carriers and not contribute to the dark current.
III. A backside mirror to duplicate IR radiation.

The above conditions may apply in heterojunction such as P^+-n-n^+ and N^+-p-p^+ with heavily doped contact regions. Homojunction devices such as n-p, n^+-p, p^+-n suffer from the excess thermal generation problem, which increases the dark current and recombination, reduces the photocurrent. The total generation rate is obtained from thermal and optical generation rates:

$$G = G_{\text{th}} + G_{\text{op}}. \tag{6}$$

By cryogenic cooling, thermal generation reaches the minimum necessary for obtaining high performance. One method to reduce the thermal generation rate is using heterodyne systems. Signal or background radiation can produce optical generation. For IR detectors, signal radiation is usually lower than background radiation. If the thermal generation is reduced much lower than the background level, the background radiation determines the device's performance (BLIP conditions for IR detectors with limited background). For more information about the theory of PDs, see Ref. 39.

4 Laser Beam Detection Based on PN Photodiodes

PN photodiodes are semiconductor devices that include a p-n junction and, in some cases, an intrinsic (undoped) layer between the p-n layers called p-i-n. Light is absorbed in the depletion or intrinsic region and generates an electron holes pair, most of which will participate in the photocurrent. The photocurrent can be proportional to the intensity of the incident light. Due to the small depletion region width in PN photodiodes, fewer photons will be absorbed, so the diode current is low, and receiver sensitivity is not optimal. On the other hand, because the width of the junction's depletion region depends on the reverse voltage, with the change in voltage, the width of the depletion region, and consequently the amount of photon absorption changes, this is not our desired dependence. In p-i-n photodiode, the depletion region is independent of bias voltage and is a low concentration doped region. PIN PDs are widely used in optical communications due to their low noise and high speed.

Some p-i-n photodiodes are silicon-based, and their sensitivity extends from visible to NIR (up to 1 μm). Their absorption and photoresponse efficiencies decrease sharply at longer wavelengths; nevertheless, their cut-off parameters depend on the thickness of the intrinsic region. InGaAs p-i-n photodiodes are available for wavelengths up to 1.7 or 2.6 μm in the extended

Table 2 Brief comparison of Si, InGaAs, Ge based photodiode made by Thorlab company.[40]

Part number	Material	Spectral range	Rise/fall time	Dark current
FDS010	Silicon	200 to 1100 nm	1 ns/1 ns @ 10 V	0.3 nA (Typ.) @ 10 V
FGA01	InGaAs	800 to 1700 nm	300 ps/300 ps @ 5 V	0.05 nA (Typ.) @ 5 V
FDG03	Ge	800 to 1800 nm	600 ns/600 ns @ 3 V	4.0 μA (Max) @ 1 V

spectral response. However, they are much more expensive especially for PDs with a larger active area. Germanium-based photodiodes can be a good alternative, but they do not respond quickly due to large parasitic capacity and high dark current. Table 2 briefly compares the Thorlab Company's p-i-n photodiodes based on silicon, InGaAs, and germanium.

From the comparison in Table 2, it is clear that Ge photodiodes are not suitable for detecting laser threats (especially LBR threats) due to their slow rise/fall time and high dark current.

In 2013, Ghuson H. Mohammed et al.[41] reported developing a p-i-n photodiode for Nd^{+3}-YAG laser detection. In their proposed structure, the detector consisted of three layers $(n^+\text{-}\pi\text{-}p^+)$ with a deep junction fabricated on a wafer with a thickness of 1 mm and a large diameter. It was observed that the peak spectral responsivity of the detector was about 1.5 A/W at a wavelength of 1.06 μm. One of the most significant features of their device is working on 170 to 180 operating reverse voltage. It should be noted that the response time of this detector is about 85 ns, which can be suitable for laser threat detection applications (except LBR threat).

In 2015, Urchuk et al. reported simulation results from the spectral sensitivity characteristics of silicon p-i-n photodiodes. It was carried out the various factors influence such as the electrons and holes lifetime and mobility, surface recombination velocity on the spectral sensitivity characteristics of p-i-n-structures. To optimize the PD structure parameters, it was calculated when changing the top layer depth of p-doping levels and changing doping areas of the structure. To expand the spectral sensitivity characteristics of silicon PD structures toward shorter wavelengths, the maximum achieving space charge region is required to the surface. At the same time, action is needed to ensure the improvement of the surface properties to reduce the surface recombination velocity and the simultaneous use of anti-reflection coatings.[42]

In 2019, Emre Doganci et al.[43] Examined the characteristics of silicon $p^+ - i - n^-$ photodiodes with 3.5×3.5, 5.0×5.0, or 7.0×7.0 mm^2 active area. Voltage–current (V-I) and capacitor–voltage (C-V) measurements were performed in the photoconductive (PC) mode to achieve the device characterizations. Both measures were carried out in a dark environment at room temperature. The measured values of the dark current (I_{dc}) and the capacitance of photodiodes were -6.97 to -19.10 nA and 23 to 61 pF at -5 V, respectively. The quantum efficiency measurements of the devices increased up to 66%. Peak responsivity was found to be 0.436 ± 1 mA/W at 820 nm. The results show that I_{dc} and device performance are improved, and therefore, this device can be used for optical electronics applications and commercial use. Experimental results showed that breakdown voltages are -93, -84, and -77.5 V for 7.0×7.0, 5.0×5.0, and 3.5×3.5 mm^2 active areas, respectively.

Of all the detectors used in the SWIR region, InGaAs has the best performance due to its high efficiency and low dark current at room temperature. This type of PD can be very suitable for imaging through foggy weather in this spectral range because it can have the maximum possible detectivity. Achieving maximum detector performance for many applications depends on the proximity of the detector bandgap energy to the light intensity energy. However, the PIN detector, which has the advantage of simplicity and the absence of geometric absorption constraints, will be matched to the typical substrate by the lattice. This often means that the bandgap energy is too low or not optimal for the desired wavelength, and the energy difference will usually cause excess noise.[44]

As mentioned in the previous sections, one of the most typical sources of laser threat is Nd: YAG laser with a wavelength of 1064 nm and, in some cases, Yb: YAG laser with a wavelength of 1030 nm.[14] However, there is a lack of high performance (low noise, high responsivity, high speed) PDs that can be operated at either of these wavelengths. Infrared-enhanced silicon

PDs have a long wavelength cutoff at or below 1030 nm. The indirect bandgap of silicon necessitates very thick absorption layers to achieve even modest efficiencies, limiting these detectors' operating speed, resulting in a low bandwidth-responsivity product. $In_{0.53}Ga_{0.47}As$ PDs (compatible with InP substrates) can achieve very high quantum efficiencies and cutoff frequencies but require growth on InP substrates, which are smaller, more expensive, and more fragile, and require a less mature process than GaAs substrates.[45]

Although Ge-based PDs can achieve very high speed due to the high mobility of the hole but suffer from high dark currents and low shunt resistors due to a very small bandgap. As a result, detectors based on this material will be very noisy at the desired wavelength. Dilute nitride semiconductors, such as InGaNAs and InGaNAsSb, are also suggested due to their ability to adjust the bandgap. Still, these compounds reduce the performance of PDs due to the relatively low quality of materials and are not suitable. $In_xGa_{1-x}As$ With low composition ($x < 0.25$), metamorphic grading can ideally meet our needs due to the direct and adjustable bandgap.

In 2011, Swaminathan et al.[46] reported the growth and performance of a top-illuminated metamorphic $In_{0.2}Ga_{0.8}As$ PIN PD on a GaAs substrate using a graded InGaAs buffer. This PD showed a very low dark current $(1.4 \times 10^{-7}\ A/cm^2)$ in -2 V reverse bias at room temperature. They showed responsivity and special detectivity values of 0.72 A/W, $2.3 \times 10^{12}\ cm \cdot Hz^{\frac{1}{2}}/W$ and 0.69 A/W, $2.2 \times 10^{12}\ cm \cdot Hz^{\frac{1}{2}}/W$ are achieved for Yb:YAG (1030 nm) and Nd:YAG (1064 nm) laser wavelengths at -2 V, respectively. At a wavelength of 1064 nm, the product of bandwidth responsivity was obtained 0.21 GHz from theoretical analysis. Their work was a turning point for adjustable bandgap gallium detectors that could grow on the gallium substrate and be used in many practical applications.

In 2015, Michael Verdun et al.[47] studied the dark current components of thin-film InGaAs PIN photodiodes grown by metalorganic vapor-phase epitaxy for optical nano-resonators. Due to the electric field enhancement, the nano-resonators made it possible to significantly reduce the thickness of the active region up to 100 nm while maintaining the quantum efficiency of the PD. In this study, to cover a broad spectral band, they combined several resonance peaks induced by guided-mode resonances in a given spectral range. This type of geometry allowed them to place the InAlAs alloy at the edge of the thin InGaAs active region to reduce the generation/recombination and diffusion currents significantly. In this design, it is observed that the components of tunnel dark current increase with decreasing the thickness of the active layer and dominate the reverse dark current. By optimizing the epitaxial stack, while keeping its total thickness constant (the optical properties of the nano-resonator remained unchanged), they showed that they could achieve a specific detectivity of up to $1 \times 10^{13}\ cm\sqrt{Hz}\,W^{-1}$ for $\lambda = 1.55\ \mu m$.

In 2019, Rutz et al.[48] reported using a planar process technology from InGaAs/InP-based PIN photodiodes to fabricate SWIR cameras with 640×512 pixels capable of capturing LLL. One of the most arrogant features of this structure was the dark current densities below $10^{-7}\ A/cm^2$ at room temperature.

Optimizing the performance characteristics (response time, dark current, and responsivity) of III-V material-based PDs has always been one of the most popular topics for scientists and researchers. One of the suggested solutions is to use nanowires based on III-V group materials due to their one-dimensional morphology, direct and tunable bandgap, and unique optical and electrical properties. Li et al.[49] studied the latest status of this type of PD.

5 Laser Beam Detection Based on Avalanche Photodiodes

There have been extensive studies, optimization, construction, and commercialization of APDs in educational, industrial, and military centers.[50] Compared to p-i-n photodiodes, APDs will have more considerable gain, higher sensitivity, and lower detection limit. For this reason, they show better performance in optical communication. The urgent need for advanced 3D imaging in laser detection and ranging (LADAR) applications have led to the use of this kind of PD structure in focal plane arrays (FPA).[51–53] Using these detectors in FPAs will have advantages, such as internal photoelectric gain, small size, low driving voltages, high efficiency, and fast response, making it possible to create 3D imaging methods and, subsequently, more detailed information to identify the object. Lincoln Laboratory at the Massachusetts Institute of Technology (MIT) is one of the most important centers that has made significant progress in this field. They improved the

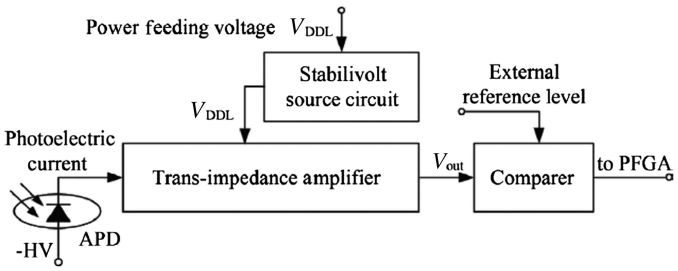

Fig. 5 Schematic of linear-mode Si APD.[53]

most advanced and state-of-the-art Si FPAs, the Giger-mode InGaAs, and applied them to some LADAR systems. Another center that has done extensive research in this area and achieved good results is Princeton Lightwave, which has succeeded in producing FPAs based on single-photon APDs and has used it in commercial cameras.

5.1 Linear-Mode Si APDs

The operation of LADAR imaging systems is based on the spatial or temporal sampling of information from optical beams to an array of detectors. LADAR systems often desire linear-mode (applied bias slightly lower than the breakdown voltage) APDs because their slow time is usually much shorter than that of Geiger-mode (applied bias somewhat higher than the breakdown voltage) APDs can measure sequential pulse returns from closely spaced multiple objects. In extreme cases, linear-mode APDs can even detect a few photons or a single photon, adding an extra dimension to LADAR scene data. In general, in the NIR spectral band, especially at 905 nm, Si APDs might be applied for ultra-weak light detection and used in linear-mode at gains up to about 500 or greater. Therefore, linear-mode Si APD arrays were developed and involved in LADAR systems.

As shown in Fig. 5, a simple linear mode APD detector will consist of an APD element (convert the incident light into photo-generated carriers and photocurrent and then amplify the resulting photocurrent through the avalanche gain by impact ionization) and a readout integrated circuit (ROIC). The ROIC consists of a trans-impedance amplifier (TIA) (converts the amplified current of the APD to a voltage signal that is proportional to the total multiplied charge delivered by the APD), a stabilivolt source circuit, and a comparator.[53]

It is important to note that in silicon; much more electrons can be ionized than holes. Therefore, instead of holes, electrons should be swept in regions with a larger electric field where multiplication occurs, which is done by the electric field.

Therefore, there should be a π-type absorption region with a suitable width for absorbing incident beams. The radiation should be able to enter this region without loss in any n^+ layer (Fig. 6).

5.2 Geiger Mode Si APD

Geiger mode APDs can detect a signal as weak as a single photon and are usually termed single-photon avalanche detectors (SPAD) (Figs. 7 and 8). The use of these adequate detectors in array

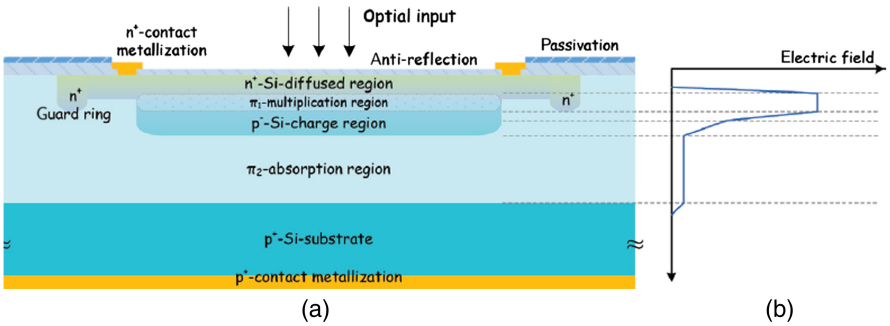

Fig. 6 (a) Schematic cross-section and (b) profile of electric field of typical APD.[53]

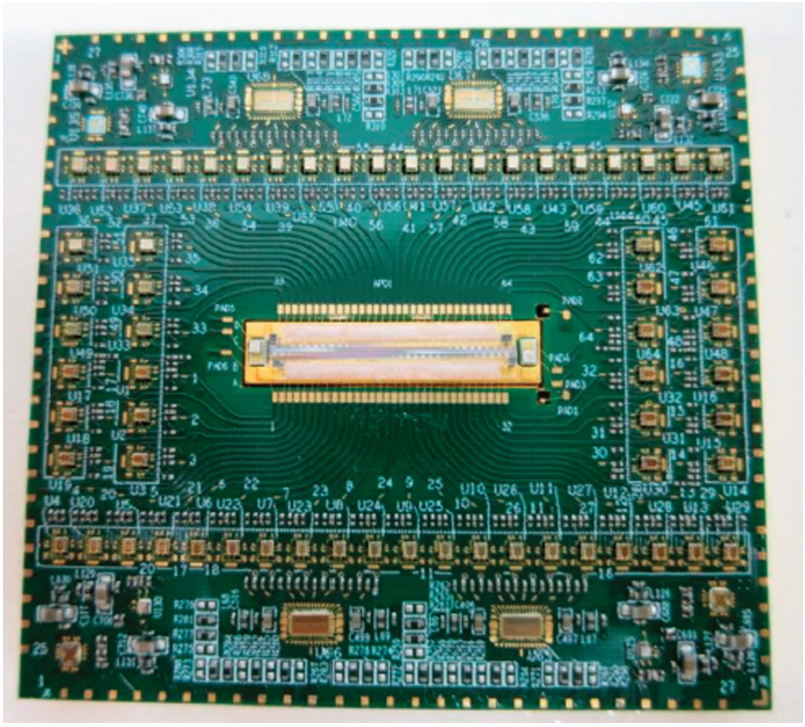

Fig. 7 64×1 linear mode Si APD FPA.[53]

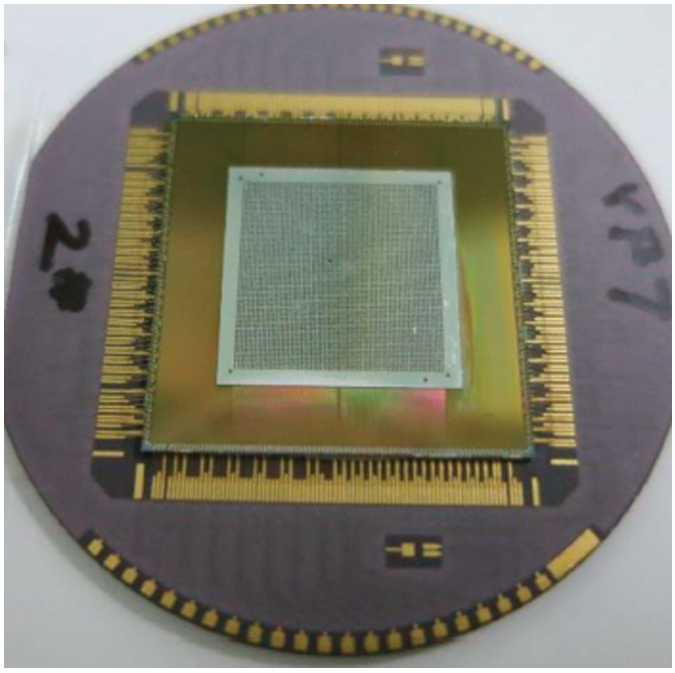

Fig. 8 One chip of Si SPAD array.[53]

configuration in applications such as LADAR and mobile laser imaging is undeniable. Hai-Zhi[53] developed Si-based SPAD arrays with the n^+-π-p-π-p^+ layers using some special processing working at 905 nm. The multiplication region of this structure is very fragile compared to the entire depletion region. Photo-generated carriers will be multiplied by the region with the highest electric field, called the multiplication region. Other parts of the depletion region may have a weak electric field, but this field must be large enough to ensure that the carrier drives at

saturation speed. As a result, the operating voltage can drop dramatically. It is important to note, two types of host materials can be used in this structure, one is a high-resistive p-type Si wafer doped by the boron (10^{14} cm^{-3}) and, the other is epitaxial lowly doped p-type Si on a p^+-doped Si wafer (Fig. 8).[53]

5.3 InGaAs APDs

The first high-performance APDs structure for the SWIR was separate absorption, charge, and multiplication (SACM) APDs made from the InP multiplication and lattice-matched $In_{0.53}Ga_{0.47}As$ absorption layers. These APDs had a good detection sensitivity up to a bit rate of 10 Gb/s InP/InGaAs. However, the relatively high k-value (directly related to excess noise) of InP caused excess noise. Recently, Nada et al. reported a receiver sensitivity of −21 dBm at 25 Gb/s and 10^{-12} bit error rate (BER) using AlInAs/InGaAs APDs at a value of $k = 0.2$.[54] However, for the past 30 years, Si has been the leading material for high-performance APDs with a k value of 0.02.[55,56] However, as mentioned in the previous section, the bandgap of this material is suitable for detecting wavelengths less than 1 μm (905 nm). In recent years, a lot of research has been done to achieve the gain characteristics of Si in the SWIR. One such approach is to combine the Ge absorption region with the a-Si multiplication layer in SACM APDs. This type of APD performs well compared to the best III-V group compounds but is not ideal due to its small k. The lattice mismatch between Si and Ge will cause a high dark current that contributes enough noise to offset the lower excess noise factor. Maddox et al. in the Department of Electrical and Computer Engineering at the University of Virginia and Microelectronics Research Center at the University of Texas designed a detector structure based on $Al_xIn_{1-x}As_ySb_{1-y}$ grown on a GaSb substrate. The excess noise factor of the multiplication region was characterized by a 0.01 value of k, which is less than the value in Si. Further, the lattice-matched absorption region has expanded the operating wavelength up to 1.6 μm and created more than 100 gain. These APDs combine Si gain/noise characteristics with low-dark current and high-speed III-V based APDs.[57]

For narrow-band gap materials such as InGaAs, high tunneling current limits their efficiency.

The separation of absorption and multiplication layers can eliminate this defect.[58] InGaAs are often used to absorb light with a wavelength of 1.55 μm, while $In_{0.52}Ga_{0.48}As$ (known as InGaAs) is a good material for the multiplication layer. InAlAs is a good electron multiplication material for InGaAs APD structure with separate absorption and multiplication APD (SAM APDs). This is due to the low energy factor of the electron ionization threshold (1.9 to 2.2 eV) and its high ionization coefficient rate from electron to hole compared to hole to the electron in InP and its small excess noise factor.[59,60] For separate absorption, grading, charge, and multiplication APDs (SAGCM), an essential element in regulating the electric field distribution in the device, which is done by changing the thickness and doping concentration of the charge layer and multiplication. It is provided that the electric field in the multiplication region is large enough. Under this condition, the carriers will suffer an avalanche, and the device will act as an APD that we like. The SAGCM APDs structure allows us to control the charge layer and the multiplication layer (thickness and impurity concentration) independently.

Chen et al. reported a two-dimensional (2D) simulation of an InGaAs/InAlAs SAGCM APDs structure. They studied the effect of charge and multiplication layers on the operating voltage ranges of the APD. They found that the punch-through voltage increases with increasing thickness and doping concentrations from the charge and multiplication layers. With increasing two-layer doping concentrations and the thickness of the charge layer, the breakdown voltage decreases. As the thickness of the multiplication layer increases, the breakdown voltage will first disappear and then rise slowly.[61]

In 2016, Woodson et al. reported a low-noise APD made of $Al_{0.7}In_{0.3}As_{0.3}Sb_{0.7}$ alloys grown on a GaSb substrate. The bandgap energy and cut-off wavelength were similar to Si. Still, due to the direct bandgap, its absorption depth is 5 to 10 times less than that of Si with an indirect bandgap, significantly increasing the bandwidth. Besides, unlike other III-V material-based APDs that operate in NIR or visible spectrum, its excess noise factor is smaller than Si ($k = 0.015$). Besides, the vast array of absorption regions is compatible with the GaSb substrate, which will cause the cut-off wavelength to vary from 1 to 12 μm.[62]

As mentioned, one of the advantages of APDs over pin photodiodes is that they are more sensitive, which is due to the multiplication property in the detection mechanism of this type of structure. By changing in the multiplication area of this type of PD, this sensitivity can be increased and used to detect weak signals. In 2013, George William et al. reported on the design, fabrication, and testing an InGaAs-based APD detector for wavelength applications between 950 and 1650 nm. This detector was grown by MBE method on the InP substrate from the lattice-matched InGaAs and InAlAs alloys (Fig. 9). Avalanche multiplication occurs in a series of asymmetric gain steps whose layer ordering acts to enhance the rate of electron-initiated impact ionization and suppress the rate of hole-initiated ionization when operated at low gain. The multiplication steps are cascaded in series, interfering with the relaxation layers where the electric field is low, and preventing feedback between the multiplication steps. These measures reduce the excess noise multiplication and the mode of stable linear operating at higher avalanche gain than the APD specifications made of the same semiconductor alloys in bulk materials. The devices that use this design work in more than 6000 linear modes without avalanche breakdown. Excess noise is also characterized by an effective impact ionization rate below 0.04 at gains of over 1000.[63]

Many military weapons applications use 10.6 μm CO_2 lasers. A mid-wavelength infrared (MWIR) APD will be used to detect this wavelength. Sensitive MWIR PDs also allow for better transmission through common atmospheric problems, such as fog, clouds, and smoke, with a glance toward applications in free-space optical communication. Besides, these devices are very suitable for detecting weak optical signals in passive imaging due to long-range applications benefiting from the superior transmission of MWIR light through common atmospheric issues.

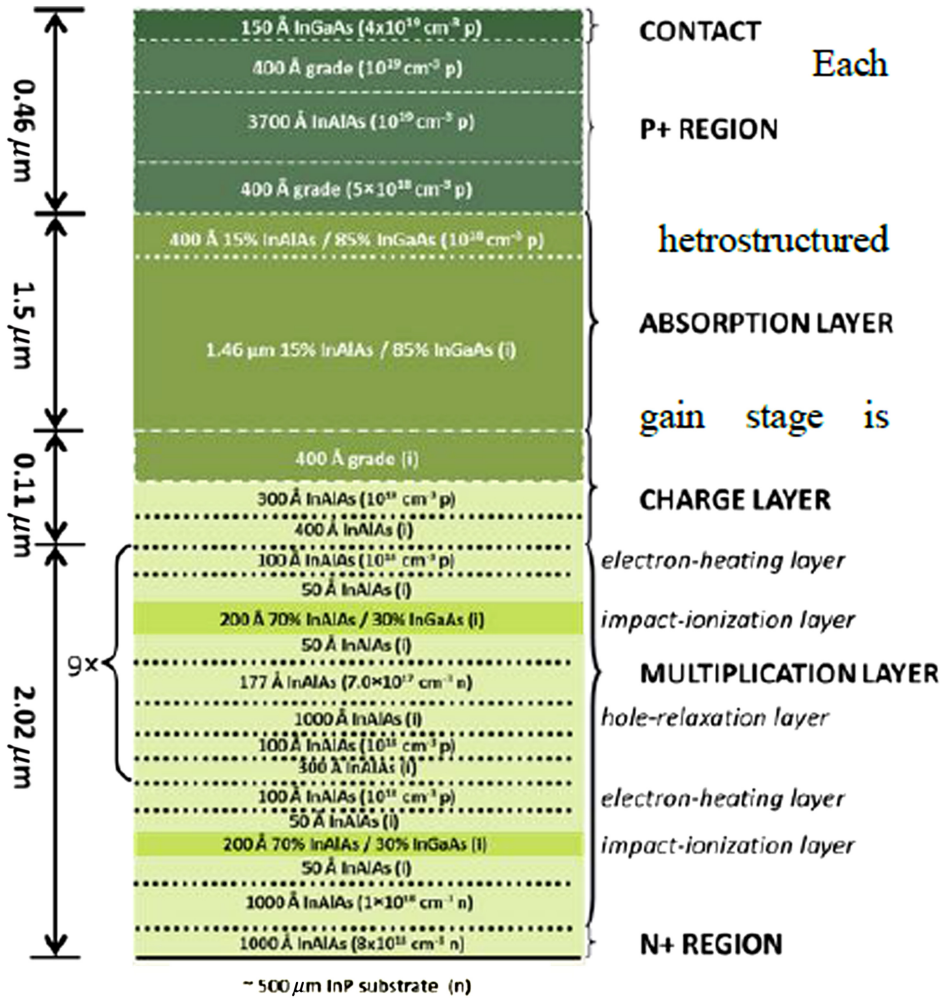

Fig. 9 Epitaxial layer structure of an SCM APD with 10 gain stages.[63]

For MWIR APD devices, the HgCdTe-based system is a good choice and can cover the whole IR spectrum range with high efficiency and low excess noise factor. However, this detection system suffers from surface instability, higher prices for fabrication, and commercialization. InAs is another good option for this detection system with an acceptable performance; however, the limitation of its cut-off wavelength has made it impossible for APDs based on this material to cover a wide range of IR. Sb-based III-V materials have been introduced to fabricate low dark current, high quantum efficiency, and single-carrier multiplication APDs. Sb-based strained-layer superlattices are structures that can cover the entire IR spectrum and are used as quantum well (QW) structures. The idea was first proposed by Nobel Laureate L. Esaki and Sai-Halasz in the 1970s.[64] Various designs based on the superlattice structure have been used for different types of high-performance devices. One of the newest structures was designed by Manijeh Razeghi at the Center for Quantum Devices, Department of Electrical and Computer Engineering, Northwestern University. Their design was based on an InAs/InSb superlattice. This device was a homojunction structure grown on a GaSb substrate. The MWIR APD is a p-i-n device with the ability to amplify internal charge carriers with an avalanche process under the high reverse bias that can cause impact ionization. The absorption region of the structure is expanded in MWIR spectral range with a gain of six at 150° K. Their research aimed to find out whether it is possible to achieve a superlattice structure based on III-V materials based on Sb for high performance of APD. It shows a 100% cut-off wavelength of 4.6 μm at 150° K and 4.3 μm at 77° K. The response of the part at 150 and 77 K has reached 2.49 and 2.32 at 3.75 μm under bias-100 V. This device of the electron-dominated avalanche mechanism with a gain value of 6 in 150 K and 7.4 in 77 K under a bias of −6.5 V has shown itself (Fig. 10).[65]

In 2019, Amiri et al. studied the effects of temperature and spectral changes on various structures of APDs. The characteristics and performance of Si, GaAs, and InGaAs APDs were examined under the influence of different temperatures. The effects of varying temperature levels on bandgap energy, detector responsivity, NEP, cut-off wavelength, dark current, and photocurrent were studied. Besides, these detectors' SNR and the BER were calculated and measured under the influence of different temperatures and spectral changes. Their proposed model was analyzed by MATLAB software, and they found that the experimentally measured results were consistent with the calculated analysis results. They discovered that InGaAs APDs performed better than other structures at higher SNR and lowered BER at higher temperatures. They realized that temperature had little effect on GaAs performance, so using these APDs in applications with higher temperatures and warmer environments is better. The energy of the bandgap decreases with increasing temperature. It has been observed that reverse bias voltage, incident beam power, an optical signal wavelength affect the quality and performance of the PD significantly. Appropriate operating parameters such as higher reverse bias voltage, higher impact power, and optical window with minimal attenuation and zero losses should be selected to

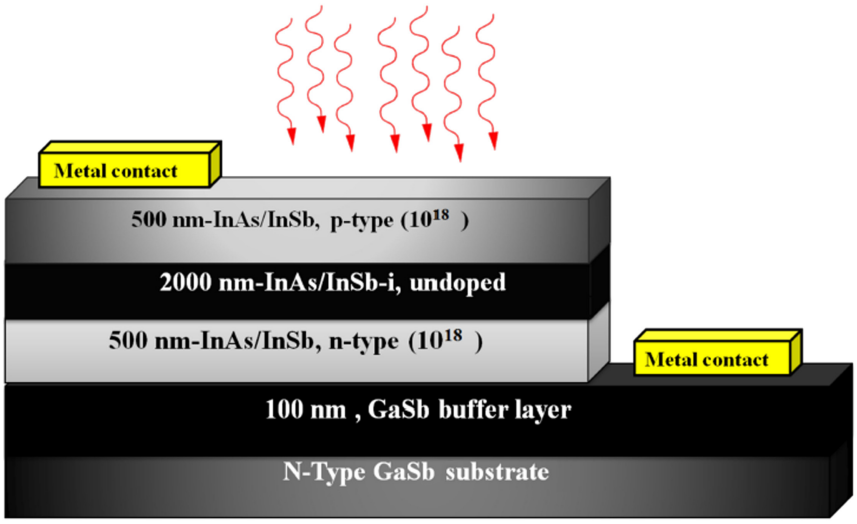

Fig. 10 Schematic of MWIR APD structure under top illumination.[65]

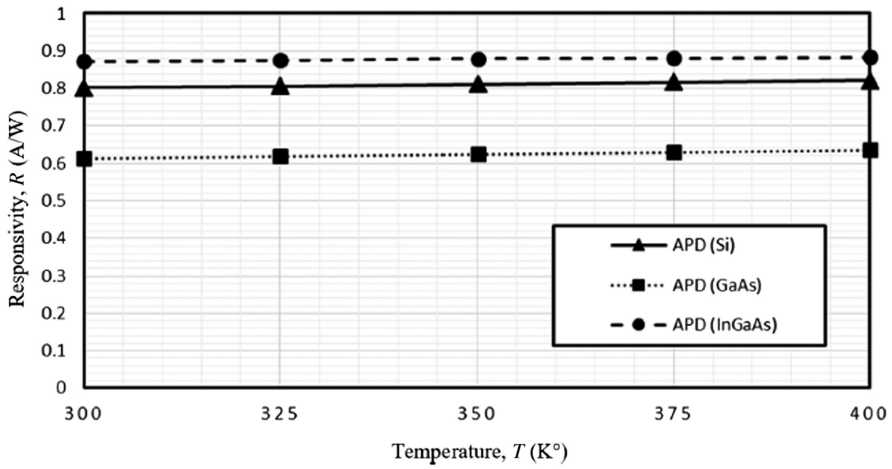

Fig. 11 Responsivity (A/W) of Si, GaAs, and InGaAs APDs structures at different levels of temperature.[66]

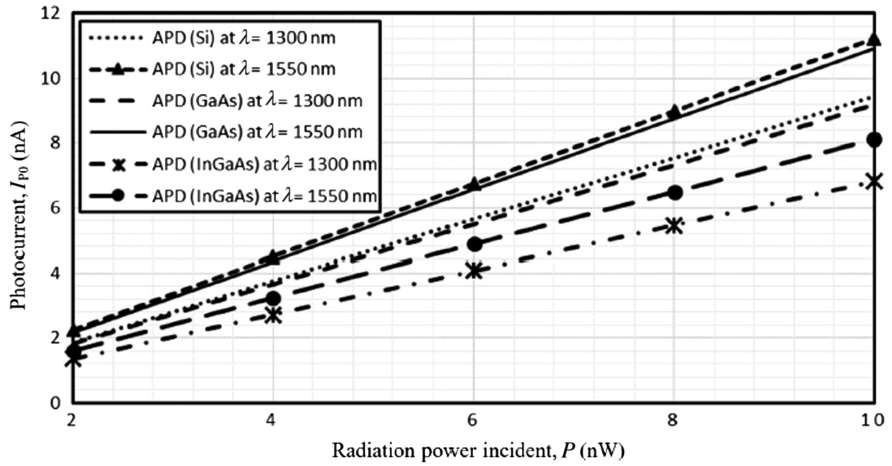

Fig. 12 Photocurrent of Si, GaAs, and InGaAs APDs for operating wavelengths 1300 and 1550 nm at different radiation power incident.[66]

achieve better system performance. Incident power can be increased by a small amount instead of increasing the reverse bias voltage to maintain good system performance. See Ref. 66 for more details (Figs. 11 and 12).

5.4 HgCdTe APDs

II-VI materials-based systems such as mercury-cadmium-telluride (MCT or MgCdTe) are the most prevalently used material for IR detection in the region of 1 to 25 μm. Some of the MCT characteristics make it a suitable material for IR detectors, which will be listed below:

5.4.1 *Adjustable bandgap (0.7 to 25 μm)*

Due to the semi-metallic nature of $Hg_{1-x}Cd_xTe$ the bandgap can be adjusted with a deviation of Cd composition in a wide range (0.3 eV for HgTe up to 0 eV for Cd composition and 1.608 eV for CdTe).

5.4.2 *Direct bandgap with a high absorption coefficient*

$Hg_{1-x}Cd_xTe$ has a direct bandgap that increases the absorption coefficient, which means no need for a thick active layer. A thin active layer will reduce the thermal generation and noise generated by excess carriers.

5.4.3 *Average dielectric constant and index of refraction*

HgCdTe has a moderate dielectric constant, making it a suitable material for integrating with circuit elements without increasing the RC constant. The effect of this characteristic can be seen in the response time, which is in the range of several nanoseconds.

5.4.4 *Average coefficient of thermal expansion*

There have been numerous reports of coefficient of thermal expansion (CTE) for HgCdTe as a function of Cd concentration at room temperature. Skauli et al.[67] provided comprehensive experimental data. CTE in the epitaxial layers of HgCdTe and its deviation with temperature play an essential and fundamental role in IR applications CTE mismatch between the HgCdTe layers and the substrate or HgCdTe layers in the neighborhood from high growth to low operating temperatures can lead to severe performance reduction or failure due to excessive thermal pressure. CTE of HgCdTe is relatively low in the entire range of alloy composition at room temperature. It has a weak positive correlation with Cd concentration.

5.4.5 *Availability of wide bandgap lattice-matched substrates for epitaxial growth*

$Hg_{1-x}Cd_xTe$ bandgap is a function of the alloy composition of x from CdTe to HgTe, and it depends on the material temperature. One of the equations is developed by Hansen to obtain the bandgap of this triple alloy:[68]

$$Eg = -0.302 + 1.93x - 0.18x^2 + 0.832x^3 + 5.35(1 - 2x)10^{-4}T. \tag{7}$$

Figure 13 shows the above equation's dependence for the alloy composition, $x = 0.2$, 0.3, and 0.4, which extend across the medium to high IR wavelength range (3 to 14 μm). As we can see, higher values of x lead to shorter wavelengths in the responsivity corresponding to the CdTe bandgap.

Scott[70] measured the HgCdTe optical absorption coefficient in a wide range of alloy compositions. The strong optical absorption of HgCdTe PDs allows us to absorb a large amount of the radiation, while the detector structure is relatively small and thin (below 20 μm). For reducing the volume of material, the thickness of the detector should be minimum, and this reduction in volume will minimize noise generation and excess carriers in the diffusion-limited operating mode.

A series of HgCdTe based APD have been characterized by diagnostic/retrieval systems technologies for light-detection and range finding applications in short and medium IR wavelengths. The results show more than 90% quantum efficiency, a gain of 600 or more, bandwidths between 6 and 7 MHz, and 0.5 NEP. The APD gain was sufficient to attain shot-limited noise performance at low-level signals. The detector has an analog linear output with a 550 dynamic range without APD and resistive trans-impedance amplifiers (RTIA) gain adaptation or signal averaging. When the APD and RTIA gain were adjusted, the linear dynamic range was more than

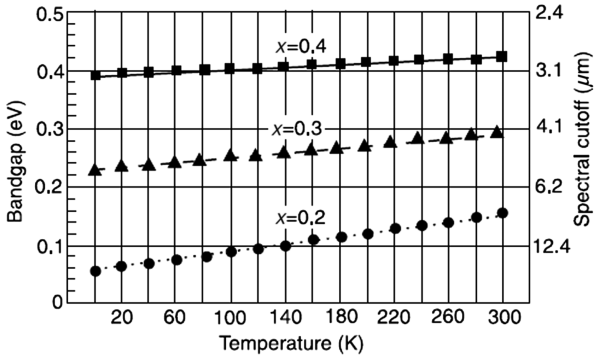

Fig. 13 Bandgap and the corresponding wavelength for alloy compounds $Hg_{1-x}Cd_xTe$ as a function of temperature as calculated from Eq. (1).[69]

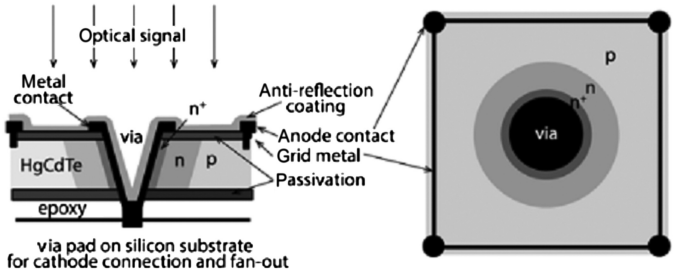

Fig. 14 Schematic illustration of the HDVIP HgCdTe APD: (a) side view and (b) top view.[71]

five times higher. The detector set was used successfully on NASA Goddard Space Flight Center (GSFC) receivers for airborne operations. These detectors will be critical for sensitive light detectors in the short and medium IR wavelengths. Figure 14 shows a simulated high density vertically integrated photodiode (HDVIP) detector.[71]

The HDVIP structure has advantages such as:

(1) Thermal cycle credibility that is independent of array size;
(2) Interdiffused CdTe passivation of both surfaces of the HgCdTe films;
(3) Low defects as a result of diode junction orientation concerning filature dislocations; and
(4) Front-side illumination for high quantum efficiency.[71]

Notwithstanding the advantages of high detectivity, high quantum efficiency (more than 70%), and fast response time (a few nanoseconds), MCT-based IR detectors have limitations. The most important of these problems is fabrication challenges due to the high pressure of Hg. Hazardous because of Cd, high prices, restrictions on the size of the FPA, and low operation temperature are other problems. Due to the above limitations, we will look for alternative materials and structures. The structure will include lead salt alloys, quantum-dot, QWs detectors, InSb, and type II superlattice-based detectors (T2SL). A large number of studies have been done on these structures.[72–78] The other designs are PbSnTe; an IV-VI compound system studied in parallel with HgCdTe from the late 1960s and early 1970s. Limitations in this structure, such as significant thermal expansion coefficient and high dielectric constant of PbSnTe compared to HgCdTe that was not compatible with Si, made this system abandoned.

Static dielectric coefficient ε_0, in PbTe is about 400[79] and 1770 in SnTe.[80] The HgCdTe IR technology still will be used due to its high performance. Nevertheless, it has its specific problems and challenges, which we mentioned below:[81]

(1) Controlling of p-type doping
(2) Larger FPA size and lower cost
(3) Higher operating temperature (HOT)
(4) Multi-band detection
(5) Advanced plasma dry etching control

6 Laser Beam Detection Based on Photoelectromagnetic Detectors

One of the most critical sources of laser threats on modern battlefields is the use of lasers at a wavelength of 10.6 μm. Undeniable LWIR detectors are needed to diagnose and characterize this type of threat. In addition to PC detectors and photodiodes, two types of contactless devices will be used for uncooled IR detectors, such as PEM and Dember effect detectors. These detectors will be used in high-speed response applications.[19]

Series of PEM detectors work on the effect of PEM on semiconductors. (The generation of an electric current in an intermetallic semiconductor in a magnetic field by the action of light.) These devices are usually optimized for the best performance at 10.6 μm. The detector consists of an MCT-based active element with an engineered bandgap with a selective composition and

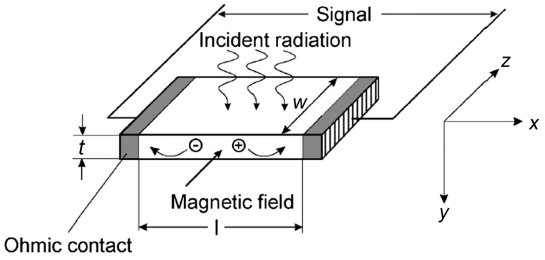

Fig. 15 Schematic of PEM effect.[82]

selective doping profile and a small permanent magnet to generate a magnetic field. Exhibiting no flicker noise will allow these detectors to be used in CW detection and the low frequency modulated radiation in the range of 2 to 11 μm simultaneously. The PEM effect was used primarily for InSb room temperature detectors in the MWIR and LWIR bands for a long time. However, the uncooled InSb devices with the cutoff wavelength at $\approx$7 μm exhibits no response in the 8 to 14 μm atmospheric window relatively average performance in a 3 to 5 μm window. $Hg_{1-x}Cd_xTe$, $Hg_{1-x}Zn_xTe$, and $Hg_{1-x}Mg_xTe$ alloys make it possible to use PEM detectors at any specific wavelength.[82]

The diffusion of photogenerated carriers will create the effect of PEM due to the photo-induced carrier in depths concentration gradient and by the deflection of electron and holes paths in different directions by the magnetic field (Fig. 15). If the two ends are open-circuit in the X direction, a space charge will be created to increase the electric field along the X-axis (open circuit voltage).

If the two ends are short-circuited in the X direction, a current will flow across the short circuit (short circuit current). Unlike PC and PV devices, PEM photovoltage (photocurrent) generation does not require simple photogeneration but instead forms an in-depth gradient of photogenerated carriers. Usually, this will be done by producing nonhomogeneous optical generation due to the radiation absorption in the area near the part's surface. The advantages of this detection structure can be:

- Ambient operating temperature
- No need for bias
- Spectral range 2 to 11 μm
- The time constant of 1 ns or less
- No flicker noise
- Performance from DC to V
- Lightweight and ease of use low price
- Typical design according to request

One of the PEM structures used to detect 10.6 μm radiation is based on a single crystal with an x composition of 0.16 to 0.17, and $Eg = 0.1 - 0.11$ eV at 300 K. In 2004, Gaziyev and Huseynov reported the results of an improvement and review of an MCT-based uncooled PEM detector of $x = 0.2$ and a bandgap of 0.155 eV for the medium IR range (3 to 7 μm).[83] The calculated results show the specific voltage response and detection versus the doping surface of the semiconductor for this detection structure. The optimal level of an acceptor doping of the semiconductor is about $p = 5 - 6n_i$ for an uncooled PEM detector. They showed that the voltage responsivity and the specific detectivity are $R_{\lambda\,\max} \approx (0.8 - 1.0)$ V/W and $D^*_{\lambda\,\max} = \approx (0.8 - 0.9)10^8$ cm $Hz^{1/2}W^{-1}$, respectively, and the sensitivity makes about 60% of the maximum responsivity of $\lambda \approx 6.7$ μm.

In 2011, Jafarzadeh and Hazrati optimized a special detector from an uncooled MCT-based PEM detector for a wavelength of 10.6 μm and an atmospheric window of 4 μm. They solved the carrier transfer equations with the Poisson equation in an external magnetic field in a self-consistent process. For 10.6 μm, the obtained optimum values of Cd molar fraction (x), applied magnetic field (B), the thickness of semiconductor (d), and the acceptor doping (Na) are $x = 0.165$, $B = 1.5$ T, $d = 4.2$ μm, $Na = 1.4 \times 10^{23}$ cm^{-3}, respectively. By taking these values

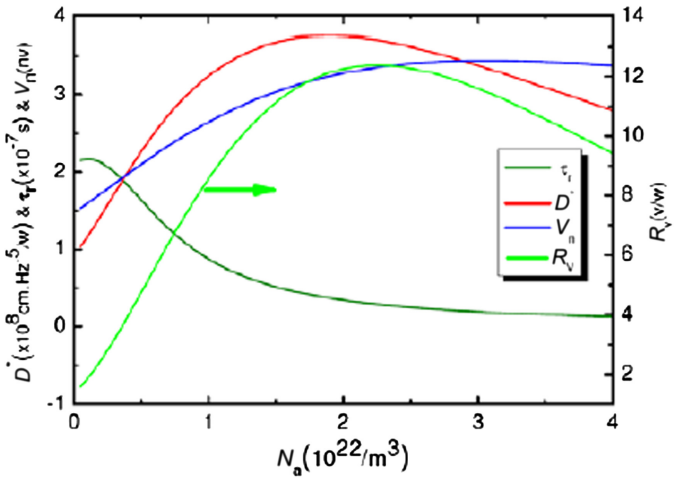

Fig. 16 Specific detectivity, responsivity, noise, and response time versus acceptor concentration for 4 μm wavelength[84] ($x = 0.308$, $l = w = 1$ mm, $d = 25$ μm, $B = 1$ T).

into account, the maximum value of specific detectivity is 3.5910^7 cm.Hz$^{1/2}$ W^{-1}. Also the responsivity (R_v) and response time (τ_r) are 0.28 V/W and 1.2 ns. For the wavelength of 4 μm, the maximum value of detectivity is and aforementioned values are: $x = 0.308$, $d = 25$ μm, $Na = 1.9 \times 10^{22}$ cm^{-3}, =12.14 V/W, =0.369 μs.[84]

Figure 16 shows the variation of the detector parameters versus the acceptor concentration. Initially, these parameters raise with increasing acceptor concentration and will reach a maximum value. Further increase of this doping will reduce these parameters, and the reason is the changes of Auger 1 and Auger 7 with the acceptor concentration.

7 Laser Beam Detection Based on Photodiffusion (Dember Effect) Detectors

Another structure used in laser threat detection is Dember effect detectors. This type of detector is a type of PV device based on bulk photodiffusion voltage in a simple structure with only one kind of semiconductor doping supplied with two contacts. When radiation strikes the surface of a semiconductor, electron and hole pairs are produced. Because of the difference in the diffusion of electrons and holes, a potential difference usually occurs in the radiation direction. The electric field in the Dember effect prevents electrons with higher mobility while the holes accelerated. Hence, both fluxes will be equal. Theoretical design of and practical Dember effect have been reported. The best performance is achieved for a device with a thickness slightly larger than the ambipolar diffusion length. More thin devices show a lower voltage responsivity, while thicker devices have excessive resistance and significant related Johnson noise. Figure 16 shows the responsivity, detectivity, and bulk recombination time for an optimized thickness Dember detector. One of the exciting aspects of this device is its impressive photoelectric gain, more considerable with a zero bias condition (Fig. 17).

By using the interference effect, the Dember effect detectors can be achieved faster and with better performance. The use of optimized optical resonance cavities for uncooled Dember detectors can increase the detection by five times for non-interfering devices. HgCdTe Dember detectors have found application in high-speed laser beam diagnostics of industrial CO_2 lasers and other applications that require fast operational speeds.[82]

8 Quadrant Photodetector in Laser Warning System

Obtaining the angle of incidence (AOI) radiation is one of the crucial expectations from LWSs. Different ideas will be used to achieve this importance. One of these ideas is using 4-QD. A QD consists of four active detection areas separated by a small gap on a single chip (Fig. 18). This detector can measure small changes in the location of the incident beam and will be used to detect the location of laser beams and position displacements.

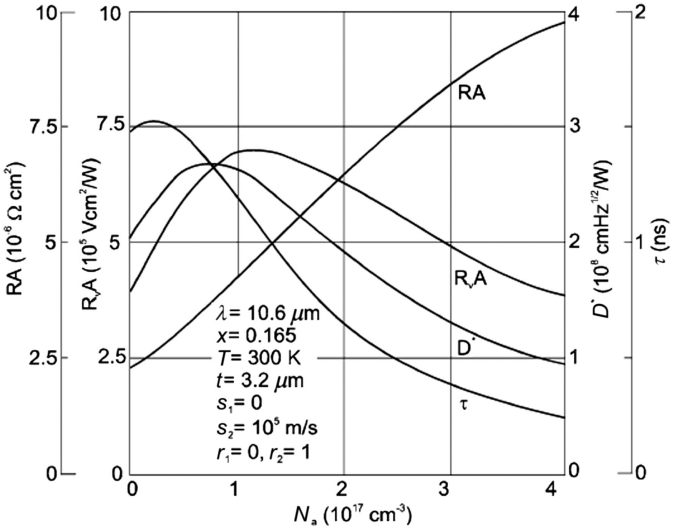

Fig. 17 Calculated normalized resistivity (RA), normalized responsivity (R_vA), detectivity (D^*), and bulk recombination time (τ) of an uncooled 10.6 μm $Hg_{1-x}cd_xTe$ Dember detector as a function of the acceptor concentration.[82]

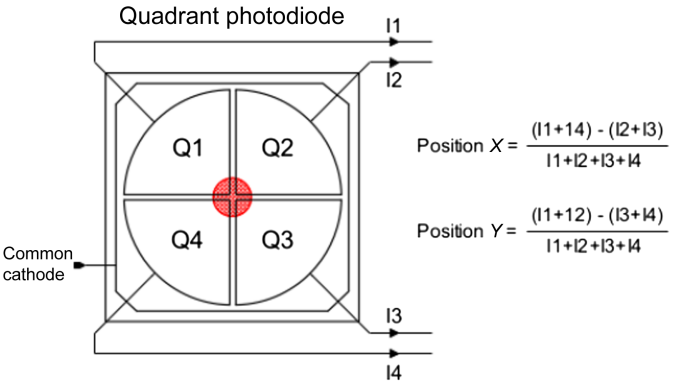

Fig. 18 Quadrant PD.[27]

In a 4Q-based laser beam detection and tracking system, the detector is usually placed on the focal length of imaging lenses to measure the laser spot displacement.[85] One of the disadvantages of beam detection methods by 4-QDs is the blind area at the photosensitive surface, affecting the position accuracy.[20] Of course, when this photosensitive surface is small enough, this blind area is negligible. Otherwise, the blind area cannot be easily ignored. In LWSs based on 4-QDs, received power ratios and associated photocurrents allow evaluating input radiation angle. This solution suffers from disadvantages, such as low and limited FOV, low angular accuracy, and strong radiation beam distribution dependence.[27]

Usually, in many applications, conventional algorithms will be used to detect the spot location in 4-QDs from an ideal circular spot with a uniform energy distribution, which has the advantage of simplicity in calculations. However, in reality, the energy distribution in a circular mode is not ideal and is usually Gaussian. Hence, the Gaussian radius and the centroid of the measuring spot are affected accurately in actual measurements. Many studies have improved the detection algorithm and location of these types of detectors.[22] Zhang et al.[86] proposed that the detection accuracy of a QD was related to the spot radius, spot position, and the QD output SNR. Wu et al.[87] analyzed the nonlinear characteristic of a QD and proposed a linear correction method based on the Boltzmann function. Gao[88] calibrated the absolute spot position and the ratio of the photocurrent output from a QD and then established a database. However, establishing a database requires a large amount of data, which involves many hardware resources.

In 2018, Jun Zhang et al. improved the spot energy distribution model to fit the elliptical Gaussian distribution. The width of the blind area has been added to the detector response model

so that the output of each quadrant and the tracking algorithm error can be calculated correctly. Their simulation results show that the accuracy of quadrant measurement decreases with increasing blind area, shape, and point of slight deviation.[85]

On the battlefield, the protection of moving assets (war machines) will be an important goal. These assets must have an LWS based on a laser tracker. In 2019, Wugang Zhang et al. proposed an improved method for detecting point location in a laser tracker and location system by a 4-QD. This method will use a 4-QD to receive the spatial information of the laser point, which will be returned to the moving target and adjust a 2D galvanometer to change the laser direction. Then the tracking function will be achieved.[89]

9 Laser Warning System Based on Multi-Color Infrared Photodetector

In the last few years, one of the areas that attracted researchers' interest in improving the detector's performance, especially for detecting objects and imaging under varying atmosphere conditions, was multicolor detectors. Since different wavelength regions are set aside for a particular empirical application, exposing an IR beam of an object at different wavelengths can be used to reduce the number of false positives.[90] The performances of two-wavelength detectors in the terahertz and mid-IR regions are inspiring.[91] Several processes enable us to have a multi-wavelength response. One of these approaches is to construct several stacks of square QW with different peak responses.[92–94] Other approaches have used asymmetric or coupled QW structures to transition from zero states to several excited states.[95,96] In this approach, only a set of QW is needed, making the manufacturing process more straightforward. In this case, photogenerated carriers will be extracted by controlling the bias voltage across the device.

Ye and Campbell[97] proposed a multi-wavelength IRPD, which is controlled with bias. Its active area consists of five layers of InAs quantum dots (QDs) with InGaAs cap layers. The photoresponse peak is observed at 5.5, 5.9, 8.9, 10.3, and 10.9 μm. The applied bias will control the relative amplitude of these peaks. For 5.9 μm detection, a peak detectivity, $D*$, of 5.8×10^9 cm $\mathrm{Hz}^{1/2}$ W at 77 K and 0.3 V was achieved.

Ali Rostami et al. presented a structure based on the quantum cascade, and it can detect two different wavelengths simultaneously across two independent current paths. This structure consists of two paths (right and left) that can detect any specific wavelength in its active region.[98]

Nguyen et al. presented spectral response characteristics of a dual-band IRPD based on nBn structure with GaSb and InGaAsSb absorbent layers and a ternary layer of AlGaSb, which acts as a unipolar barrier layer and is independent access to both sides (Fig. 19). The results show the spectral response in the short-range IR region, especially in the wavelength of 1.6 and 2.65 μm,

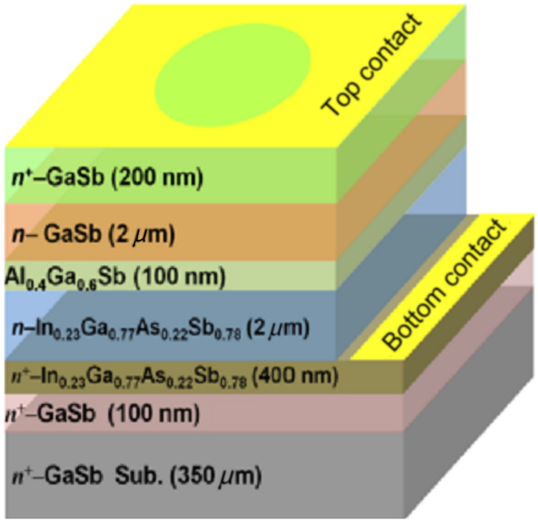

Fig. 19 Layer structure of IRPD.[99]

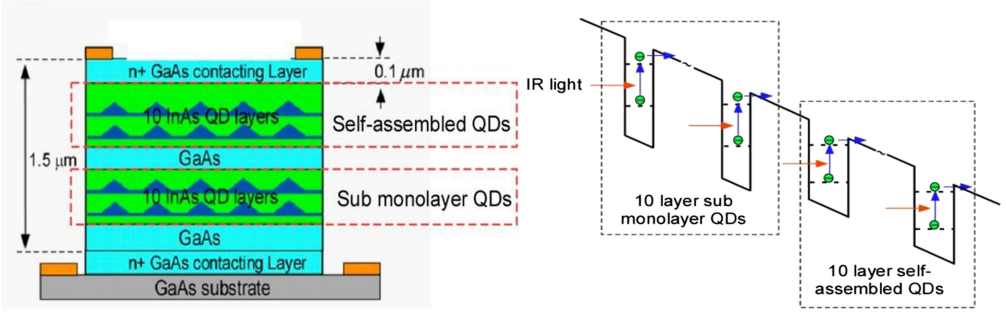

Fig. 20 (a) Schematic structures of the hybrid QDIP. (b) Conduction band structure of the SML and self-assembled QDIP.[100]

which is voltage bias dependent. D^* values are 2.3×10^{12} cm.Hz$^{1/2}$.W^{-1} (at 1.5 μm) and 2.1×10^{11} cm.Hz$^{1/2}$.W^{-1} (at 2.25 μm) at 300 K.[99]

Yao Zhai et al. proposed a dual-band PD in the mid and long IR regions. This PD is capable of voltage-controllable detection. This structure is based on multiple stacks of sub-monolayer (SML) QDs and self-assembled QDs. The detection band in MWIR, or LWIR, or both with high photodetectivity and low crosstalk between the bands will be achieved by varying the detector voltage bias. The schematic of this structure is shown in Fig. 20.

As we can see, this structure consists of 10 layers of SML QDs and 10 layers of self-assembled QDs sandwiched between the top and bottom contact layers. The electrons will be collected by the top and bottom electrodes, forming a photocurrent. The QDs sizes and the energy levels are unalike due to different strains informing. Thus, allowing them to detect various bands. By optimizing the QD growth conditions, such as substrate temperatures, growth rate, and the V to III ratios, the detection of the MWIR and the LWIR bands will be achieved. The growth of strain-driven band structure engineering offers an alternative way to achieve dual-band PDs.[100]

10 Image Sensors Based Laser Warning System

The use of imaging elements in LWSs is also prevalent. Imaging LWSs will include fisheye lenses to provide a high FOV, narrowband spectral filters, and imaging components.[101] Because the imaging element is so small, it can accurately orient the laser threat. In the past decade, due to the limitations of CMOS technology, CCD cameras have been used more for LWSs. With the advancement of CMOS technology, these cameras took advantage of advantages, such as high integration, low power dissipation, high speed, and good radiation resistance, which led to the use of these cameras in this application.[102] One of the challenges in CMOS-based LWSs is the effect of the fill factor on the exact location of the laser spot. When the laser spots fall on the CMOS element, the non-photosensitive area of the CMOS element will cause the laser spot to be missing.

If we consider a laser beam that is an ideal point (Fig. 21) (impact function) on the focal plane through the lens of the fisheye and the laser spot distribution, we have the following relation:

$$I(x,y) = \frac{I_0}{2\pi\sigma_{\mathrm{PSF}}^2} \exp\left(-\frac{(x-x_c)^2+(y-y_c)^2}{2\sigma_{\mathrm{PSF}}^2}\right), \tag{8}$$

where I_0 is the total energy of the laser spot, (x_c, y_c) is the energy center of the laser spot, σ_{PSF}^2 is the Gauss radius. The PSF radius can be calculated by $r = 1.22\lambda f'/D$, where λ is the laser wavelength, f' is the focal length of fisheye lens, and D is the aperture of the fisheye lens.

In addition, we assume that the CMOS imaging device consists of two parts: photo-electricity conversion (photosensitive) and electro-circuit control (non-photosensitive). In that case, the fill factor is the ratio of the photosensitive area to the whole imaging element. It should be noted that the fill factor for CMOS is between 30% and 70%.

In 2009, Jiaju Ying et al. analyzed the effect of the fill factor on the exact location of a laser spot in an LWS. The locating standard deviation was performed by Monte Carlo simulation,

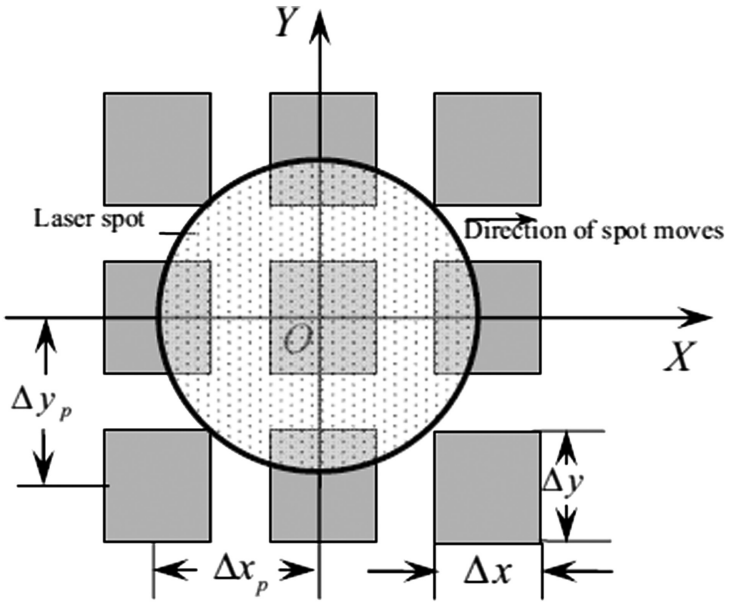

Fig. 21 Distribution of image elements array and laser spot.[103]

and an experiment was performed to confirm this simulation. It has guiding value for analyzing the orientation precision and selecting the parameters of the CMOS sensor and fisheye lens, when imaging LWS is built up.[103]

Yas A. Alsultanny reported the analysis of helium–neon (He-Ne) laser profiles and a laser diode. He showed that the He-Ne laser emits a pure Gaussian beam while the laser diode emits elliptical shape beam. This report analyzes the intensity of distribution, laser power, and the number of possible modes necessary for many applications. Image profile analysis can determine the distance between objects, depending on the laser beam line distribution. The block diagram of this setup is shown in the figure below (Fig. 22).[104]

In 2016, Alistair developed a method and device for detecting lasers in an LWR. In this invention, a set of panoramic lenses used in cameras is combined with a laser focal plane (Fig. 23). Collision laser light is refracted in panoramic lenses to create several single sensor elements. By determining the corresponding intensity of the laser light on the sensors, the angle of arrival (AoA) resolutions superior to the part angular resolutions can be achieved. Combining a panoramic lens with a laser detection focal plane provides a low-cost laser warning for wrap-around ground-based situational awareness.[105]

Some LWS configurations use the diffraction grating method to measure wavelength and AOI. The advantage of using diffraction grating is the simultaneous measurement of wavelength and incident angle. Figure 24 shows that this receiver will consist of a linear CCD camera,

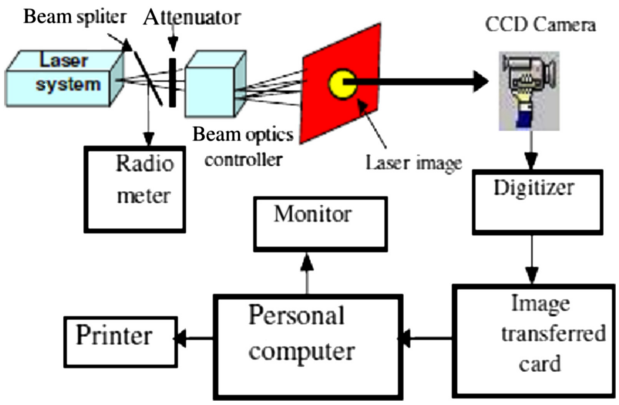

Fig. 22 Block diagram of laser beam profile analysis.[104]

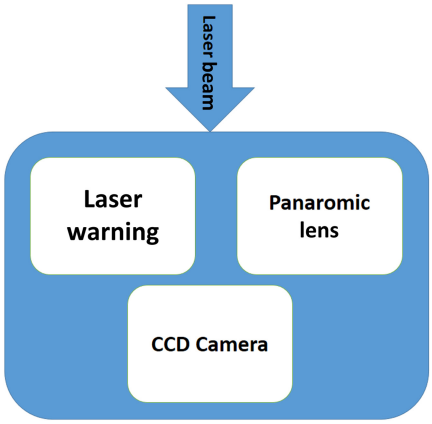

Fig. 23 Illustration a block diagram of a panoramic LWR.[105]

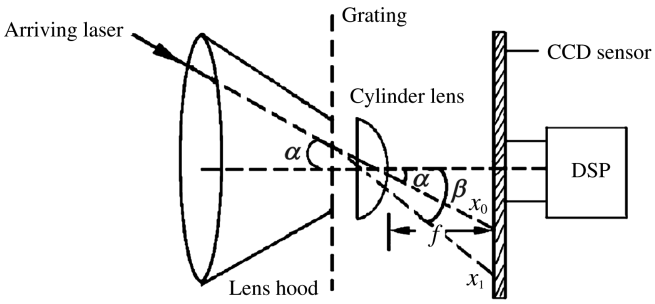

Fig. 24 Principle of sinusoidal grating LWR.[106]

a plane-convex cylinder lens, and a sinusoidal grating. The beam strikes the grating at λ wavelength and α angle. After scattering by the grating and focusing on the lens, two diffraction patterns will be formed. These two diffraction patterns will be converted into an electrical signal by the CCD camera and then into the processing unit. See Ref. 106 for more information.

11 Nanostructures to Enhance the Electronic Characteristics of Infrared Detectors

Imagers and IR sensors using nanostructure-based materials are being advanced for various defense applications.[107] Engineering the electronic characteristics of the absorbent material to reach high quantum efficiency and detectivity is one of the methods to enhance the performance of PDs (the product of bandwidth detectivity). Increasing the light coupling to electronic states of absorbent material is another method. Both of these methods can be implemented using micro and nanofabrication techniques.[81]

11.1 Infrared Detectors Based on Quantum Wells

QWs and superlattices are the oldest nanostructures to improve quantum efficiency. Although, among the different types of QWIPs, GaAs/AlGaAs QWs detectors will be further studied due to a closely complete lattice match between GaAs and AlGaAs.[77,108–113] Devices based on GaAs/AlGaAs QWs have advantages such as:[114]

(1) It can be built with GaAs standard manufacturing methods.
(2) Very high uniformity and coherent growth of the permeability controlled on 6-in. GaAs wafers.
(3) Very low $1/f$ noise.
(4) High efficiency and low cost.
(5) High thermal stability.
(6) External radiation firmness.

11.2 Infrared Detectors Based on Quantum Dots

The desire to have IR detectors at high temperatures, higher efficiency, and lower prices made it possible to look for smaller quantum dimensions than QWs. QDs will participate in different material systems and increase the quantum efficiency and system temperature. The most widely used QDs in IR detectors include QDs based on III-V materials[115–117] and Si and Ge-based material. QD-based detectors are similar to QWs based detectors but have many advantages over QWs, due to the confinement of the three dimensions of this nanostructure. One of these advantages is that QDs are intrinsically susceptible to IR radiation due to breaking the polarization selection rule.[118]

Lower dark current due to the weaker thermionic emission is another advantage of using QDs in detector structure that results from the confinement of the carriers in three dimensions.[119]

The discrete energy levels in the QDs do not disperse. This attribute reduces the phonon dispersion, leading to an increase in carrier lifetime (greater than 100 ps) and increasing the temperature of the operation.[120]

The detection mechanism in QD IR detectors is based on the intersubband transitions between the continuum states and quantized energy levels.[121] However, these detectors have less absorption quantum efficiency due to the small fill factor in the QD and significant inhomogeneous broadening of the self-assembled QDs. This inhomogeneous expansion will make it harder to adjust the precision of some wavelengths, which ultimately leads to problems with strain and dislocations with increasing the absorption layers and reduce the absorption coefficient.

One of the most widely used structures that have improved the response performance, detectivity, dark current, and temperature of the IR detectors is sandwiched QD layers with the current barrier layers $Al_{0.3}Ga_{0.7}As$.[122,123]

Another structure used for QD IR detectors is the quaternary In (Ga) As/GaAs QDs. To acquire QDIP with a minimum dark current (maximum detectivity), an uncoupled InGaAs/GaAs QD heterostructure was proposed. The dots were capped with a thick combination barrier including, a 30 Å layer of quaternary $In_{0.22}Al_{0.22}Ga_{0.58}As$ and a 500 Å layer of GaAs. This thick barrier was united into the QD heterostructure to interrogate carrier tunneling in bordering dot layers at a high temperature and estimate the concurrent lowering of the dark current. Using the In (Ga) As/GaAs QDs, a two-color IR detector with a response of ~2.16 A/W at 77° K and a detectivity of 1.01×10^{11} cm $Hz^{1/2}$/W obtained. Then, using the InAs/GaAs QDs, a multi-color IR detector can achieve a broad-band wide-spectral, highly narrowed spectrum.[124]

11.3 Nanowire for Infrared Detection

High sensitivity and high anti-reflection due to anisotropic geometry and high surface-to-volume rates are unique electronic and photonic characteristics of semiconductor nanowires (NW).[81] The NW energy band can be modified by engineering on semiconductor materials due to advanced nanostructure fabrication methods. Much research has been accomplished on nanowire-based detectors.[125–128] The III-V semiconductor nanowires with a narrow bandgap are a good choice for making IR detectors. IR detectors based on InAs, InP, InGaAs, and InGaSb NWs reported.[125,128,129] In general, nanowire-based IR detectors can be divided into three categories. Photoconductor, phototransistor, and heterostructure NW devices, including homo-/heterojunction and Schottky photodiodes. In these types of structures, the material will be sandwiched between the two electrodes.[130] Usually, the NW PDs based on III-V compositions are more likely to be studied than other materials due to ultra-precision transitions, easy construction, and widespread wavelength adjustment by engineering the bandgap.

Furthermore, their low capacitance will result in high-performance speeds. One of the most studied compositions is InGaAs, which can adjust its wavelength from the NIR to the MIR range. In addition, the mobility of electrons is high, and the leakage current is low. For single crystal NWs $In_{0.65}Ga_{0.35}As$, the highest response rate of 6.5×10^3 A/w has been reported on a wide range of 1.1 to 2 μm.[128] The photoresponsivity of 5.3×10^3 A/w was reported in Schottky–Ohmic contacted InAs NW PDs at the wavelength around below.[131]

Another structure used for NW-based detectors is phototransistors. The phototransistor is a monopolar or bipolar transistor in which light is transmitted to the carriers, and the current can be amplified during transistor operation. Therefore, optical responsivity will be much more

significant. However, many of today's NW-based phototransistors have recombination losses; it means that carriers recombined before they can be combined. The core-shell design will solve this issue. One of the most-used phototransistors is InAs phototransistors made from an InAs nanowire with a self-made optical gate, including randomly distributed network defects, used as a trap layer to take stimulated electrons.[132] This core/shell structure, such as n-InAs, has a response time of 12 ms at 1.2 μm wavelengths.

12 Nanostructures to Enhance the Light Coupling in Infrared Detectors

By increasing the radiation flux coupling to the optical sensing medium (area), IRPD's performance can be improved. There are several ways, such as a reflective concentrator, refractive concentrator, and anti-reflective coating (AR), by which this importance can be achieved.

As we know, most semiconductors that are used for IRPDs have an extensive refractive index of about 3 to 4. Hence, anti-reflex structures are essential since about 25% to 40% of the losses are due to the reflection of the surface. Typically, the most superficial AR coating can be made by depositing one or several optically thin films on the surface utilizing interference effects to cancel the back-reflection.[133] However, this method also has limitations in that the reflection varies by changing the incident angle. Another limitation of this approach is the narrow spectral response band that provides weak coating layers in new multi-color and multi-band IR detectors. Usually, anti-reflection conditions create by placing slow-wave structures against the detector.

12.1 Resonant Cavity

By locating the active region inside the resonant cavity between resonance mirrors (usually including a reflecting mirror and a Bragg distribution mirror), the absorption within the detector will increase significantly. When the product of the thickness of the active area and effective absorption coefficient is small enough, the cavity will hold just a single optical mode, and the rest of the modes will stop. The important note about this structure is that this structure reduces the PD's speed, limited by the carrier's transmission time.[134]

12.2 Plasmonic and Nanoantenna

One of the fastest-growing research areas is the field of interaction between light matter, such as plasmonics and nanoantenna.[135] Metal or dielectric nanostructures can increase the absorption of a cross-section of light-sensitive material, usually by local electromagnetic fields within subwavelength environments. Plasmonic and nanoantenna provide a high concentration of field and strong light–matter interaction over a broad spectrum band. Light trapping schemes will be divided into two different groups using plasmonic levels for PD:[136,137]

- Localized surface plasma includes plasmonic nanoparticles or hollow nanoparticles.
- Surface plasma polariton containing various diffusion structures.[138]

The first type consists of the localization of the field and the production of critical points, plasmon-based single-element optics, and trans-based transitions, and the second type involves structures such as networks for coupling the field into guided modes and the wavelet of photonic crystals that may be periodically or quasi-periodic.[132–136]

Another structure that couples the optical waves and transient fields are nanoantennas or optical antenna. The significant changes in the momentum of the photon are unique features of these devices. Due to the type of antenna and its design, the mode limit in the field can be deeply subwavelength. Detectors based on coupled nanoantennas have been introduced as a research topic in the IR detector family. The nanoantenna will optimize energy transfer to the subwavelength localized sensor and provide irradiance gathering. The antenna shape and geometry can be tailored for given requirements, including spectral response, resonant wavelength, polarization, and angular response. Optical antennas entrap the far-field light, and its concentration in the active area will increase. Metal–oxide–metal diodes (MOM) coupled optical antennas have been used to direct radiation in the mid-IR range. The devices show reception angles of 50 deg and narrow beamwidths of ~35 deg FWHM in power.[139,140] Most of the challenges in the antenna design are due to the air–dielectric interface.[141]

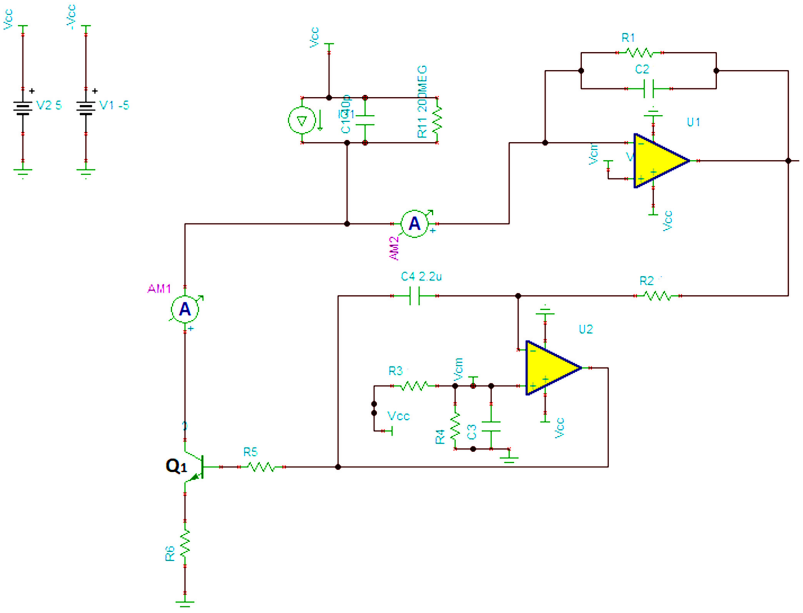

Fig. 25 Designed TIA circuit.[143]

Our group has designed a front-end circuit (TIA, DC removal, and amplification circuits) of 1 MHz bandwidth LWS capable of removing DC voltage (caused by background and solar light) in the NRC at IUST (Fig. 25). The article's introduction states that most laser threats are in the NIR range. We assumed that a laser threat with a wavelength of 905 nm hit the LWS from a distance of 1000 m. After passing through the optical subsystem (spectral filter and focusing lens), the laser beam hit the PD (part number: BPW34) and established a current of 1 μA at the output of the PD. The main task of the TIA stage (U_1) will be to convert this output current into a readable voltage in the processing subsystem. The equivalent circuit of PD is used in the circuit below, which includes the capacitor C_1 (detector junction capacity) and parallel resistance R_{11} with the current source. The feedback resistor (R_1) and capacitor (C_2) are designed for the amount of DC signal amplification and bandwidth required for the circuit. R_1 has a considerable contribution to the total noise of the system, so it is impossible to choose a significant value for this resistance. We prefer to select a 10 kΩ resistor to have an output of 10 mv ($V_{\text{out(TIA)}} = -I_D \times R_1$), after which we reach an output voltage of $1v$ with two stages of inverting and non-inverting voltage amplification with gains of 10 and 11, respectively. Friis' formulation shows system noise reduction with increased amplification stages, confirming this theory.

No matter how much the background light adds DC level to the output of our PD, the first stage (TIA) input (AM_2) will only be the laser current signal. Transistor Q_1 and Op-Amp U_2 remove the background light from the incident laser beam. The dynamic range for our circuit design is from the DC value of 0 to 23 mA, which is observed in the simulation (Fig. 26).

After two amplification stages, this signal will reach 1 V and be ready for sampling and processing. Another critical thing to simplify the circuit design is using an Op-Amp package for each detector, for which we used quad low power Op-Amp. The figure below shows the printed circuit board designed and built for a linear array of 12 sensors and its related circuits in 3D (Fig. 27).

Circuit simulation is done by Tina-TI software was made by Texas Instrument.

The values of feedback resistance and capacitor along with the value of the junction capacity of the PD and the input capacitors of the Op-Amp in common and differential modes play a fundamental role in frequency analysis and bandwidth. It is desirable to use Op-Amps with FET input. For how to analyze and design, you can use the website of Texas Instrument Company.

In LWSs, most innovations are done regarding detecting the threat beam and the AoA resolution, and the front-end circuits will be less addressed.[12,22,26,27,103,142] However, the reduction of system noise will primarily be related to the design of the front-end circuit. Using improved

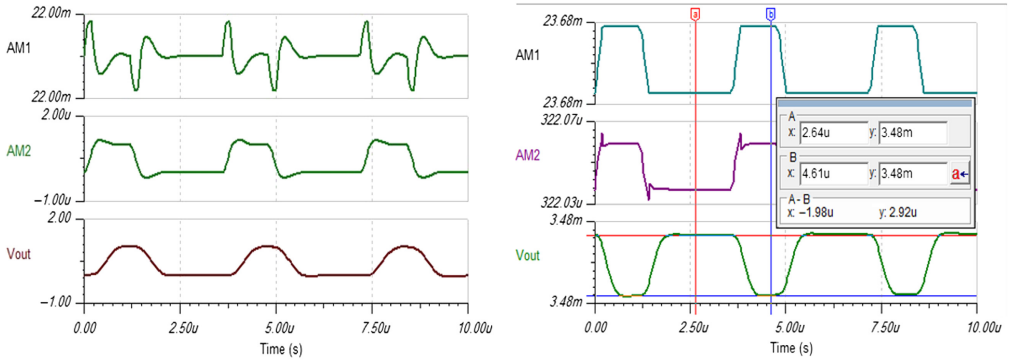

Fig. 26 Illustration of the dynamic range in the designed circuit. (a) The correct output value when the DC level is 22 mA and (b) incorrect output value when the DC level is 23 mA.[143]

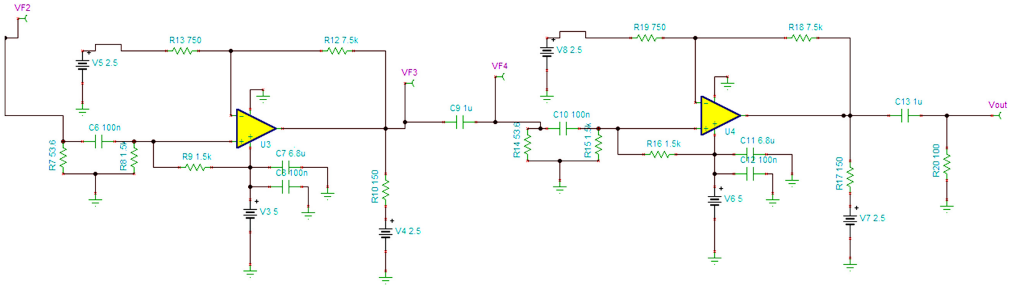

Fig. 27 Amplification stages.[143]

Table 3 Comparison of the products of some manufacturing companies with our own designed system.[143]

Product name (company name)	Wavelength range	AoA resolution	Power dissipation
SAPLAR 4C-22L-6R-12G (ELECTRO OPTIC COMPONENTS)[150]	400 to 1700 nm	15 deg	Max. 65 W
LW100 (Neroindustries)[151]	500 to 12,000 nm	1 deg	120 ± 50 mA 24VDC
ATLAS-2Q (Hensoldt)[152]	500 to 1650 nm	2 deg	N/A
Optronics LWS (Thales)[153]	400 to 1600 nm	15 deg	15 W for four arrays
ISTEC[154]	700 to 1100 nm	22.5 deg	4 W single detector
Our design	500 to 1550 nm	8 deg (90-deg horizontal coverage with 12 sensors)	13.85 mv per detector

transistor topologies with very low-power telecommunication transistors or using more precise Op-Amps with higher gain-bandwidth products and lower input noise density can help to reduce the noise of the whole system.[144–149]

Saab, Hensoldt, Elbit system, Neroindustries, Thales, and ISTEC are among the leading companies in manufacturing LWSs. In Table 3, we compare some of the specifications of these companies' products with our own designed system.

One of the advantages of our designed circuit will be the simplicity of the circuit and, at the same time, its efficiency, which can simultaneously receive multi threats from a linear detection array by a unique algorithm applied in the processing subsystem (Fig. 28). It is also essential to

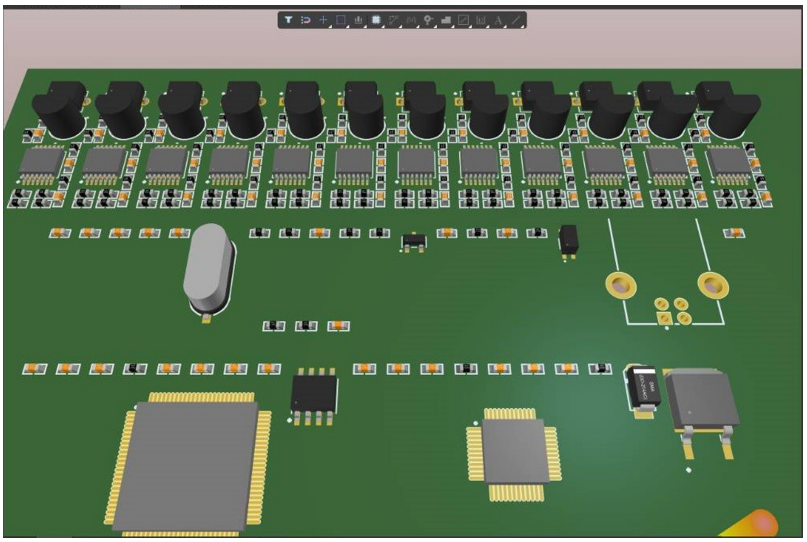

Fig. 28 3D illustration of front-end designed circuit.[143]

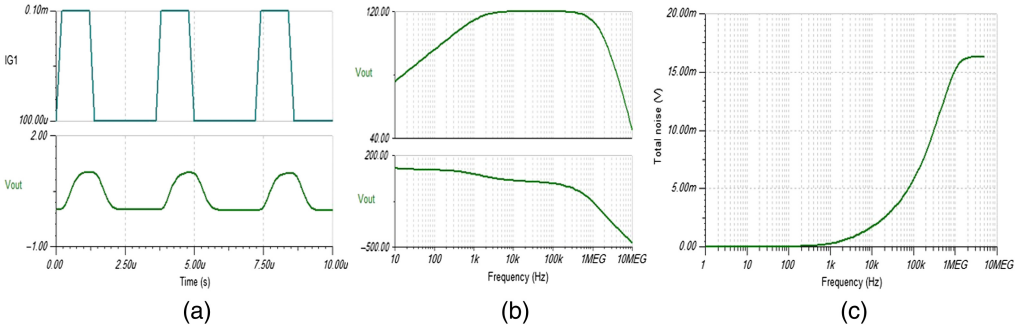

Fig. 29 (a) Output waveform, (b) circuit bandwidth, and (c) total noise of the circuit.[143]

state that the amount of noise in the entire system is negligible compared to the output voltage, which does not interfere with sampling our output signal (Fig. 29).

In Table 4, we reviewed some of the designed and manufactured characterizations of LWSs.

13 Conclusion

Due to security threats and electromagnetic interference affecting RF, the use of visible and IR beams using lasers has become an integral part of today's battlefields. Low divergence and laser beam coherence provide a secure data transmission. Laser threats can use any wavelength in the IR region. The most common will be in the NIR range and can be detected at short intervals (about 10 ns). Hence, as one of the subsystems of LWSs, IR detectors must have the best performance (response time, low dark current, and responsivity). Depending on the azimuth and horizontal coverage axis and the accuracy of the angular resolution, it is possible to choose how to configure the PDs (singular mode or 2D arrays of detectors vertically and horizontally).

PIN detectors are one of the most common detectors to be used in this system and have the advantage of high speed and low noise. It was shown that the various factors influence the electrons and holes lifetime and mobility, surface recombination velocity on the spectral sensitivity characteristics of p-i-n-structures. The breakdown voltage in the detector will increase as the active area increases. In the SWIR region, InGaAs has the best performance due to their high efficiency and low dark current at room temperature. PIN PD on a GaAs substrate using a graded InGaAs buffer showed a very low dark current. The product of bandwidth-responsivity was obtained 0.21 GHz from theoretical analysis, which is very suitable for this particular application. For narrow-band gap materials such as InGaAs, high tunneling current limits their efficiency. InGaAs APDs performed better than other structures at higher SNR and lowered BER at higher

Table 4 Reviewing some designed LWSs.

Title	Year	Optical subsystem	Detection subsystem	FOV (accuracy)	Other features
Improved miniaturized HARLID for LWSs having high angular resolution[155]	2001	Gray Code Maskair light guide channels	Si and InGaAs linear arrays (500 to 1700 nm) sandwich configuration	±15 elevation (0.7 deg)	2 ns response time
Research on coherent LWR based sinusoidal transmission grating diffraction[106]	2006	Sinusoidal transmission amplitude grating, a plant convex cylinder lens	A linear CCD with 50 MHz driving frequency (500 to 1100 nm)	22.5 in latitude or longitude (1 deg)	Responding time < 0.1 s detecting sensitivity <10 mW/cm^2
A new design for LWS[31]	2007	Optical antenna, fiber bundle, plano-convex lens with a convex, and planar surface	Non-scanning Michelson interferometer, the Fourier-transform lens, cylindrical lens, 1D CCD	45 deg in azimuth	Discriminating narrow laser pulse
Detecting modulated lasers in the battlefield and determining their direction[28]	2009	Sinusoidal grating, lens, Fizeau interferometer	2D PD array	—	Estimation for low light levels with lenses
Design of an LWS using an array of discrete photodiode.[12]	2011	Focusing lens	8 × 4 InGaAs PD array	360 deg in azimuth 35 deg in elevation (3 deg)	Solve the dead zone problem
Panoramic LWR for determining AoA of laser light based on intensity[105]	2016	A panoramic lens assembly combined with a laser detection focal plane, relay lens	CCD, element hexagonal APD array	360 deg in azimuth 87 deg in elevation	—
A new advanced design and implementation of LWS[21]	2018	Focusing lens	4 quadrant detector	360 deg in azimuth	CW or pulsed laser detection and low FAR
Developments in low-cost laser detection: wide FOV implementation and directiondetermination[29]	2019	Cone mirror	Mach–Zehnder interferometer, camera, Si photodiode (350 to 1100 nm)	360 deg in azimuth	Sensitivity below 100 nW
Freeform mirror design for novel LWRs and laser AOI sensors.[27]	2020	Freeform mirror, high-numerical-aperture, fully achromatic f-theta lens, perfectly focusing lens	Linear array of photodiode (41 discrete PIN PDs arranged in a cross-plan)	90 to 120 deg	Reduced stray light; _ a higher dynamic range

temperatures. It has been observed that reverse bias voltage, incident beam power, an optical signal wavelength affect the quality and performance of the PD significantly.

The adjustable bandgap, direct bandgap with a high absorption coefficient, average dielectric constant and index of refraction, the average CTE, and availability of wide bandgap lattice-matched substrates for epitaxial growth made MCT suitable material for IR detectors. PEM and Dember effect detectors are usually optimized for the best performance at 10.6 μm. The blind area at the 4-QD photosensitive area will affect the position accuracy. By adding the width of the blind area to the detector response model, each quadrant's output and the tracking algorithm's error are calculated correctly. Two methods to have multiwavelength PD are several stacks of square QW with different peak responses and asymmetric or coupled QW structures to transition from zero states to several excited states. With a linear CCD camera, a plane-convex cylinder lens, and a sinusoidal grating simultaneous measurement of wavelength and incident angle can be obtained. QD-based detectors are similar to QWs based sensors. Still, they have many advantages over QWs, due to the confinement of the three dimensions of this nanostructure and the weaker thermionic emission (lower dark current). High sensitivity and high anti-reflection due to anisotropic geometry and high surface-to-volume rates are unique electronic and photonic characteristics of semiconductor nanowires. By locating the active region inside the resonant cavity between resonance mirrors (usually including a reflecting mirror and a Bragg distribution mirror), the absorption within the detector will increase significantly. Plasmonic and nanoantenna provide a high concentration of field and light–matter strong interaction over a broad spectrum band.

Availability Statement

The data supporting this article's findings are not publicly available due to privacy and ethical concerns. They can be requested from the authors at shahramm@iust.ac.ir or msm_electro.1988@yahoo.com.

References

1. A. David et al., "Laser threat warning system and method," EP 2 661 642 B1 (2017).
2. V. Coffey, "High-energy lasers: new advances in defense applications," *Opt. Photonics News* **25**(10), 28 (2014).
3. S. Affan Ahmed, M. Mohsin, and S. M. Zubair Ali, "Survey and technological analysis of laser and its defense applications," *Def. Technol.* **17**(2), 583–592 (2020).
4. G. Overton, "Boeing HEL MD high-energy laser targets UAVs/mortars even through wind and fog," (2014). http://www.laserfocusworld.com/articles/2014/08/boeing-hel-md-highenergy-%0Alaser-targets-uavs-mortars-even-through-wind-and-fog.html.
5. "Robust electric laser initiative (RELI)," U.S. Army Space and Missile Defense Command/ Army Forces Strategic Command USASMDC/ARSTRAT Public Affairs Office, http://www.northropgrumman.com/Capabilities/%0ASolidStateHighEnergyLaserSystems/ (2023).
6. M. Eckstein, "Solid state laser-technology maturation," (2020). https://news.usni.org/tag/solid-state-laser-technology-maturation.
7. "Turbulence-taming turret: Lockheed Martin prototype expands laser performance at jet speeds," (2015). https://news.lockheedmartin.com/2015-10-15-Turbulence-taming-Turret-Lockheed-Martin-Prototype-Expands-Laser-Performance-at-Jet-Speeds (2023).
8. H. Kaushal and G. Kaddoum, "Applications of lasers for tactical military operations," *IEEE Access* **5**, 20736–20753 (2017).
9. D. R. Jungwirth***Chicago, "Laser detection and warning system," 13197661.5 (2014).
10. B. Gephart, *Laser Detecting Systems, ISR & Space Systems*, UTC Aerospace Systems (2018).
11. A. Feickert, *U.S. Army Weapons-Related Directed Energy (DE) Programs: Background and Potential Issues for Congress*, 2018, Congressional Research Service, Washington, D.C. (2023).
12. R. B. S. Sushil Kumar et al., "Design of a laser-warning system using an array of discrete photodiodes—part I," *J. Battlef. Technol.* **14**(1), 1440–5113 (2011).
13. S. Mohammad Nejad, H. Arab, and N. Ronagh Sheshkelani, "Analysis of new laser warning technologies to propose a new optical subsystem," *Iran. J. Electr. Electron. Eng.* **14**, 213–221 (2018).
14. M. R. N. A. Eslami Majd, A. Naseri, and A. Masoumian, "Design and implementation of a tester system for laser warning system," *Adv. Def. Sci. Technol.* **7**(2), 107–117 (2016).
15. Excelitas Company, "Laser warning receiver," http://www.boselec.com/products/detirlwr.html.

16. "Avalanche photodiodes," https://www.excelitas.com/product-category/avalanche-photodiodes (2023).
17. OSI Optoelectronics, "Nd-YAG optimized photodiodes," https://www.osioptoelectronics.com/standard-products/silicon-photodiodes/nd-yag-optimized-photodiodes.aspx (2023).
18. H. Yuan et al., "Recent progress in extended wavelength InGaAs photodetectors and comparison with SWIR HgCdTe photodetectors," *Proc. SPIE* **11129**, 111290E (2019).
19. Photonic Solutions Ltd., "Infrared photoelectromagnetic detectors," https://www.photonicsolutions.co.uk/product-detail.php?prod=5916 (2023).
20. W. Zhang et al., "Design of small laser tracking system based on four-quadrant detector," *Appl. Mech. Mater.* **300–301**, 393–399 (2013).
21. M. Tayel, M. Shehata, and A. Almslmany, "A new advanced design and implementation of laser warning system," in *13th Int. Conf. Comput. Eng. and Syst. (ICCES)*, pp. 219–224 (2018).
22. Q. Li et al., "An improved method for the position detection of a quadrant detector for free space optical communication," *Sensors* **19**(1), 175 (2019).
23. M. B. Sinclair, "Laser warning receiver to identify the wavelength and angle of arrival of incident laser light," US 7,683,310 B1 (2010).
24. É. Desfonds, *Recent Advances in Laser Warning Systems*, 2011, Excelitas Technologies, Canada (2023).
25. T. K. Saha et al., "Design of an angle detector for laser beams based on grating coupling," *Micromachines* **3**(1), 36–44 (2012).
26. A. R. Anand Kumar Rai, S. Bansod, and S. Prakash, "Detection of angle-of-arrival of the laser beam using a cylindrical lens and Gaussian beam curve fitting," *Int. Res. J. Eng. Technol.* **6**(7), 1646–1664 (2019).
27. J. Wojtanowski, M. Jakubaszek, and M. Zygmunt, "Freeform mirror design for novel laser warning receivers and laser angle of incidence sensors," *Sensors* **20**(9), 2569 (2020).
28. A. D. McAulay, "Detecting modulated lasers in the battlefield and determining their direction," *Proc. SPIE* **7336**, 73361J (2009).
29. M. Zandi, D. M. Benton, and K. Sugden, "Developments in low-cost laser detection: wide field of view implementation and direction determination," *Proc. SPIE* **11161**, 111610H (2019).
30. A. F. El-Sherif et al., "The design and implementation of photoacoustic based laser warning receiver for harsh environments," *Opt. Laser Technol.* **98**, 385–396 (2018).
31. W. Z. Li Xiao et al., "A new design for laser warning system," in *7th WSEAS Int. Conf. Signal, Speech and Image Process.* (2007).
32. M. Al-Jaberi et al., "The simulation of laser-based guided weapon engagements," *Proc. SPIE* **6228**, 622814 (2006).
33. H. Dong, Z. Zhou, and F. Huang, "Analysis of false alarm for imaging space-based laser warning system," *Optoelectron. Lett.* **8**(2), 105–108 (2012).
34. Y. Liu, B. Tu, and L. Liu, "The energy distribution of the imaging spot in the ultra-wide field-of-view fisheye lens acquisition system," in *8th Int. Congr. Image and Signal Process. (CISP)*, pp. 722–726 (2015).
35. H. Dong and L. Wang, "Non-iterative spot center location algorithm based on Gaussian for fish-eye imaging laser warning system," *Optik* **123**(23), 2148–2153 (2012).
36. F. Hanson et al., "Off-axis detection and characterization of laser beams in the maritime atmosphere," *Appl. Opt.* **50**(18), 3050 (2011).
37. S.-H. Tang et al., "Bionic compound eye using microlens array with multi-focus and long focal depth," in *Symp. Design, Test, Integr. and Packag. of MEMS/MOEMS (DTIP)*, pp. 1–5 (2017).
38. B. Chen, Y. Chen, and Z. Deng, "Recent advances in high speed photodetectors for eSWIR/MWIR/LWIR applications," *Photonics* **8**(1), 14 (2021).
39. A. Rogalski, "Quantum well photoconductors in infrared detector technology," *J. Appl. Phys.* **93**(8), 4355–4391 (2003).
40. Thorlabs, "Ultrafast Fiber Optic Photodetector Modules, OEM Package," https://www.thorlabs.com/newgrouppage9.cfm?objectgroup_id=11975.
41. B. A. M. Al-Hilli et al., "Fabrication of silicon PIN photodiode for Nd+3-YAG laser detection," *Indian J. Appl. Res.* **3**(3), 330–332 (2011).
42. S. U. Urchuk et al., "Spectral sensitivity characteristics simulation for silicon p-i-n photodiode," *J. Phys. Conf. Ser.* **643**, 012068 (2015).
43. E. Doğanci et al., "Fabrication and characterization of Si-PIN photodiodes," *Turk. J. Phys.* **43**(6), 556–562 (2019).
44. P. Lacovara et al., "Room-temperature diode-pumped Yb:YAG laser," *Opt. Lett.* **16**(14), 1089 (1991).
45. S. Donati, *Photodetectors: Devices, Circuits and Applications*, 2nd ed., Prentice Hall (2000).
46. K. Swaminathan et al., "Metamorphic In_020Ga_080As p-i-n photodetectors grown on GaAs substrates for near infrared applications," *Opt. Express* **19**(8), 7280 (2011).
47. M. Verdun et al., "Dark current investigation in thin P-i-N InGaAs photodiodes for nano-resonators," *J. Appl. Phys.* **120**(8), 084501 (2016).
48. F. Rutz et al., "InGaAs SWIR photodetectors for night vision," *Proc. SPIE* **11002**, 1100211 (2019).

49. Z. Li et al., "Review on III-V semiconductor single nanowire-based room temperature infrared photodetectors," *Materials* **13**(6), 1400 (2020).
50. J. C. Campbell, "Recent advances in avalanche photodiodes," *J. Lightwave Technol.* **34**(2), 278–285 (2016).
51. M. Diagne et al., "Advances in InP/InGaAs Geiger-mode APD focal plane arrays (Conference Presentation)," *Proc. SPIE* **10659**, 1065904 (2018).
52. F. Ceccarelli et al., "152-dB dynamic range with a large-area custom-technology single-photon avalanche diode," *IEEE Photonics Technol. Lett.* **30**(4), 391–394 (2018).
53. H.-Z. Song, "Avalanche photodiode focal plane arrays and their application to laser detection and ranging," in *Photodetectors [Working Title]*, K. Chee, Ed., IntechOpen (2018).
54. M. Nada et al., "Triple-mesa avalanche photodiode with inverted P-down structure for reliability and stability," *J. Lightwave Technol.* **32**(8), 1543–1548 (2014).
55. R. J. McIntyre, "Recent developments in silicon avalanche photodiodes," *Measurement* **3**(4), 146–152 (1985).
56. V. M. Robbins et al., "Electron and hole impact ionization coefficients in (100) and in (111) Si," *J. Appl. Phys.* **58**(12), 4614–4617 (1985).
57. S. J. Maddox et al., "Recent progress in avalanche photodiodes for sensing in the IR spectrum," *Proc. SPIE* **9854**, 985405 (2016).
58. J. N. Haralson et al., "Numerical simulation of avalanche breakdown within InP-InGaAs SAGCM standoff avalanche photodiodes," *J. Lightwave Technol.* **15**(11), 2137–2140 (1997).
59. Y. L. Goh et al., "Excess avalanche noise in $In_{0.52}Al_{0.48}As$," *IEEE J. Quantum Electron.* **43**(6), 503–507 (2007).
60. J. P. R. David and C. H. Tan, "Material considerations for avalanche photodiodes," *IEEE J. Sel. Top. Quantum Electron.* **14**(4), 998–1009 (2008).
61. J. Chen et al., "Optimization of InGaAs/InAlAs avalanche photodiodes," *Nanoscale Res. Lett.* **12**(1), 33 (2017).
62. M. E. Woodson et al., "Low-noise AlInAsSb avalanche photodiode," *Appl. Phys. Lett.* **108**(8), 081102 (2016).
63. G. M. Williams et al., "Multi-gain-stage InGaAs avalanche photodiode with enhanced gain and reduced excess noise," *IEEE J. Electron Devices Soc.* **1**(2), 54–65 (2013).
64. G. A. Sai-Halasz, R. Tsu, and L. Esaki, "A new semiconductor superlattice," *Appl. Phys. Lett.* **30**(12), 651–653 (1977).
65. A. Dehzangi et al., "Avalanche photodetector based on InAs/InSb superlattice," *Quantum Rep.* **2**(4), 591–599 (2020).
66. I. S. Amiri et al., "Temperature effects on characteristics and performance of near-infrared wide bandwidth for different avalanche photodiodes structures," *Results Phys.* **14**, 102399 (2019).
67. P. Tomasini et al., "Growth by OMVPE and x-ray analysis of ZnTe and epilayers on III–V substrates," *J. Cryst. Growth* **166**(1–4), 590–596 (1996).
68. G. L. Hansen, J. L. Schmit, and T. N. Casselman, "Energy gap versus alloy composition and temperature in $Hg_{1-x}Cd_xTe$," *J. Appl. Phys.* **53**(10), 7099–7101 (1982).
69. P. Norton, "HgCdTe infrared detectors," *Opto-Electron. Rev.* **10**, 159–174 (2002).
70. M. W. Scott, "Energy gap in $Hg_{1-x}Cd_xTe$ by optical absorption," *J. Appl. Phys.* **40**(10), 4077–4081 (1969).
71. X. Sun et al., "HgCdTe avalanche photodiode detectors for airborne and spaceborne lidar at infrared wavelengths," *Opt. Express* **25**(14), 16589 (2017).
72. A. Rogalski, "HgCdTe infrared detector material: history, status and outlook," *Rep. Prog. Phys.* **68**, 2267 (2005).
73. T. C. Harman and I. Melngailis, *Narrow Gap Semiconductors*, pp. 1–94, Springer (1974).
74. A. Rogalski, "Infrared detectors: status and trends," *Prog. Quantum Electron.* **27**(2–3), 59–210 (2003).
75. W. Lei et al., "Interband and intraband photocurrent of self-assembled InAs/InAlAs/InP nanostructures," *Nanotechnology* **16**, 2785 (2005).
76. X.-Q. Huang et al., "Characterization of InAs quantum dots on lattice-matched InAlGaAs/InP superlattice structures," *J. Cryst. Growth* **270**(3–4), 364–369 (2004).
77. A. Haddadi et al., "$InAs/InAs_{1-x}Sb_x$ type-II superlattices for high performance long wavelength infrared detection," *Appl. Phys. Lett.* **105**(12), 121104 (2014).
78. G. H. Olsen et al., "128x128 InGaAs detector array for 1.0–1.7 μm," *Proc. SPIE* **1341**, 432 (1990).
79. Y. Kanai and K. Shohno, "Dielectric constant of PbTe," *Jpn. J. Appl. Phys.* **2**, 6 (1962).
80. P. B. Allen and M. L. Cohen, "Carrier-concentration-dependent superconductivity in SnTe and GeTe," *Phys. Rev.* **177**(2), 704–706 (1969).
81. C. L. Tan and H. Mohseni, "Emerging technologies for high performance infrared detectors," *Nanophotonics* **7**(1), 169–197 (2018).
82. A. R. Jozef Franciszek Piotrowski, "Photoelectromagnetic, magnetoconcentration, and dember IR detectors," in *High-Operating-Temperature Infrared Photodetectors*, pp. 179–196, SPIE Press, Bellingham, Washington (2007).

83. F. Gaziyev and E. Huseynov, "Photoelectromagnetic detector on the basis of $Cd_xHg_{1-x}Te$," *Solid State Electron.* **48**(9), 1679–1681 (2004).
84. R. H. Hossein Jafarzadeh, "Realization of a photoelectromagnetic detector for middle and far infrared spectral regions operating at room temperature," in *Int. Conf. Nanostructures and Nanomaterials: Science and Applications*, Islamic Azad University, Masjed Soleyman Branch and Tehran Science and Research Branch (2011).
85. J. Zhang et al., "Quadrant response model and error analysis of four-quadrant detectors related to the non-uniform spot and blind area," *Appl. Opt.* **57**(24), 6898 (2018).
86. H. Zhang et al., "Study on main factors affecting position detection accuracy of four-quadrant detector," *Chin. J. Lasers* **42**(12), 1217002 (2015).
87. W. Jiabin, Z. Bo, and W. Zhiyong, "Improved measurement accuracy of the spot position on an InGaAs quadrant detector by introducing Boltzmann function," in *Int. Conf. Optoelectron. and Microelectron. (ICOM)*, pp. 183–185 (2015).
88. Z. Gao, *Study on Vibration Characteristics Measurement Technology of Airborne Photoelectric Platform*, Dalian Maritime University (2014).
89. W. Zhang et al., "An improved method for spot position detection of a laser tracking and positioning system based on a four-quadrant detector," *Sensors* **19**(21), 4722 (2019).
90. G. Ariyawansa et al., "Multi-color tunneling quantum dot infrared photodetectors operating at room temperature," *Infrared Phys. Technol.* **50**(2–3), 156–161 (2007).
91. L. Lever et al., "Terahertz ambipolar dual-wavelength quantum cascade laser," *Opt. Express* **17**(22), 19926 (2009).
92. A. Köck et al., "Double wavelength selective GaAs/AlGaAs infrared detector device," *Appl. Phys. Lett.* **60**(16), 2011–2013 (1992).
93. K. L. Tsai et al., "Two-color infrared photodetector using GaAs/AlGaAs and strained InGaAs/AlGaAs multiquantum wells," *Appl. Phys. Lett.* **62**(26), 3504–3506 (1993).
94. Y. Zhang et al., "A voltage-controlled tunable two-color infrared photodetector using GaAs/AlAs/GaAlAs and GaAs/GaAlAs stacked multiquantum wells," *Appl. Phys. Lett.* **68**(15), 2114–2116 (1996).
95. E. Martinet et al., "Switchable bicolor ($5.5-9.0\ \mu$m) infrared detector using asymmetric GaAs/AlGaAs multiquantum well," *Appl. Phys. Lett.* **61**(3), 246–248 (1992).
96. J. Chiang et al., "A voltage-tunable multicolor triple-coupled InGaAs/GaAs/AlGaAs quantum-well infrared photodetector for $8-12\ \mu$m detection," *Appl. Phys. Lett.* **69**(16), 2412–2414 (1996).
97. Z. Ye et al., "Voltage-controllable multiwavelength InAs quantum-dot infrared photodetectors for mid- and far-infrared detection," *J. Appl. Phys.* **92**(7), 4141–4143 (2002).
98. A. Rostami et al., "A dual-color IR quantum cascade photodetector with two output electrical signals," *IEEE Trans. Electron. Devices* **58**(1), 165–172 (2011).
99. T. D. Nguyen et al., "Dual-color short-wavelength infrared photodetector based on InGaAsSb/GaSb heterostructure," *AIP Adv.* **8**(2), 025015 (2018).
100. Y. Zhai, G. Gu, and X. Lu, "Voltage-tunable mid- and long-wavelength dual-band infrared photodetector based on hybrid self-assembled and sub-monolayer quantum dots," *Micromachines* **10**(1), 4 (2018).
101. D. M. Benton, M. Zandi, and K. Sugden, "Laser detection utilizing coherence," *Proc. SPIE* **11161**, 111610G (2019).
102. K. Cabanas-Holmen, D. Dorn, and C. Tesdahl, "Characterization and system modeling of a 5-Mpixel CMOS array," *Proc. SPIE* **6501**, 65010Q (2007).
103. J. Ying, Y. He, and Z. Zhou, "Analysis on laser spot locating precision affected by CMOS sensor fill factor in laser warning system," in *9th Int. Conf. Electron. Meas. & Instrum.*, pp. 2-202–2-206 (2009).
104. Y. A. Alsultann, "Laser beam analysis using image processing," *J. Comput. Sci.* **2**(1), 109–113 (2006).
105. A. McNeish, "Panoramic laser warning receiver for determining angle of arrival of laser light based on intensity," U.S. Patent No. US9448107B2 (2016).
106. J. L. Zhang, E. M. Tian, and Z. B. Wang, "Research on coherent laser warning receiver based sinusoidal transmission grating diffraction," *J. Phys. Conf. Ser.* **48**, 800–805 (2006).
107. A. K. Sood et al., "Design and development of carbon nanostructure-based microbolometers for IR imagers and sensors," *Proc. SPIE* **7679**, 76791Q (2010).
108. C. Mailhiot and D. L. Smith, "Long-wavelength infrared detectors based on strained InAs–$Ga_{1-x}In_xSb$ type-II superlattices," *J. Vac. Sci. Technol. A Vac. Surf. Film* **7**(2), 445–449 (1989).
109. H. Schneider et al., "QWIP FPAs for high-performance thermal imaging," *Phys. E Low-Dimens. Syst. Nanostruct.* **7**(1–2), 101–107 (2000).
110. H. Schneider et al., "Photovoltaic quantum well infrared photodetectors: the four-zone scheme," *Appl. Phys. Lett.* **71**(2), 246–248 (1997).
111. F. Fuchs et al., "Optoelectronic properties of photodiodes for the mid-and far-infrared based on the InAs/GaSb/AlSb materials family," *Proc. SPIE* **4288**, 171–182 (2001).

112. M. Razeghi and B.-M. Nguyen, "Band gap tunability of type II antimonide-based superlattices," *Phys. Proc.* **3**(2), 1207–1212 (2010).
113. B.-M. Nguyen et al., "Type-II M structure photodiodes: an alternative material design for mid-wave to long wavelength infrared regimes," *Proc. SPIE* **6479**, 64790S (2007).
114. S. D. Gunapala et al., "Long-wavelength 256 × 256 GaAs/AlGaAs quantum well infrared photodetector (QWIP) palm-size camera," *IEEE Trans. Electron. Devices* **47**(2), 326–332 (2000).
115. S. D. Gunapala et al., "Demonstration of 640 × 512 pixels long-wavelength infrared (LWIR) quantum dot infrared photodetector (QDIP) imaging focal plane array," *Infrared Phys. Technol.* **50**(2–3), 149–155 (2007).
116. D. A. Ramirez et al., "Midwave infrared quantum dot avalanche photodiode," *Appl. Phys. Lett.* **97**(22), 221106 (2010).
117. S. Hellström et al., "Increased photocurrent in quantum dot infrared photodetector by subwavelength hole array in metal thin film," *Appl. Phys. Lett.* **96**(23), 231110 (2010).
118. S. Kim et al., "Growth and characterization of InGaAs/InGaP quantum dots for midinfrared photoconductive detector," *Appl. Phys. Lett.* **73**(7), 963–965 (1998).
119. V. Ryzhii, "The theory of quantum-dot infrared phototransistors," *Semicond. Sci. Technol.* **11**(5), 759–765 (1996).
120. J. Urayama et al., "Observation of phonon bottleneck in quantum dot electronic relaxation," *Phys. Rev. Lett.* **86**(21), 4930–4933 (2001).
121. J. Jiang et al., "High detectivity InGaAs/InGaP quantum-dot infrared photodetectors grown by low pressure metalorganic chemical vapor deposition," *Appl. Phys. Lett.* **84**(12), 2166–2168 (2004).
122. D. Pal and E. Towe, "Characteristics of high-operating-temperature InAs/GaAs quantum-dot infrared detectors," *Appl. Phys. Lett.* **88**(15), 153109 (2006).
123. S.-F. Tang, S.-Y. Lin, and S.-C. Lee, "InAs/GaAs quantum dot infrared photodetector (QDIP) with double Al/sub 0.3/Ga/sub 0.7/As blocking barriers," *IEEE Trans. Electron. Devices* **49**(8), 1341–1347 (2002).
124. S. Adhikary and S. Chakrabarti, "In(Ga)As/GaAs quantum dot infrared photodetectors (QDIPs) with quaternary capping," in *Quaternary Capped In(Ga)As/GaAs Quantum Dot Infrared Photodetectors*, pp. 33–45, Springer Singapore, Singapore (2018).
125. L. Ma et al., "Room-temperature near-infrared photodetectors based on single heterojunction nanowires," *Nano Lett.* **14**(2), 694–698 (2014).
126. W. Lei et al., "Optical properties of self-assembled InAs/InAlAs/InP quantum wires with different InAs deposited thickness," *J. Cryst. Growth* **286**(1), 23–27 (2006).
127. R. Basori and A. K. Raychaudhuri, "Role of contact and contact modification on photo-response in a charge transfer complex single nanowire device," *Nano-Micro Lett.* **6**(1), 63–69 (2014).
128. J. Miao et al., "Single InAs nanowire room-temperature near-infrared photodetectors," *ACS Nano* **8**(4), 3628–3635 (2014).
129. H. Tan et al., "Single-crystalline InGaAs nanowires for room-temperature high-performance near-infrared photodetectors," *Nano-Micro Lett.* **8**(1), 29–35 (2016).
130. V. J. Logeeswaran et al., "A 14-ps full width at half maximum high-speed photoconductor fabricated with intersecting InP nanowires on an amorphous surface," *Appl. Phys. A* **91**(1), 1–5 (2008).
131. H. Fang et al., "Visible light-assisted high-performance mid-infrared photodetectors based on single InAs nanowire," *Nano Lett.* **16**(10), 6416–6424 (2016).
132. A. Y. Zhang, *Silicon Nanowire Phototransistor: Designing, Fabricating and Characterizing a High Responsibility, Broadband Photodetector*, University of California San Diego (2010).
133. H. Angus Macleod, *Thin-Film Optical Filters*, 3rd ed., CRC Press, Boca Raton, Florida (2001).
134. G. W. Ju et al., "RCEPD with enhanced light absorption by crown-shaped quantum well," *IEEE Photonics Technol. Lett.* **27**(19), 2047–2050 (2015).
135. C. C. Katsidis and D. I. Siapkas, "General transfer-matrix method for optical multilayer systems with coherent, partially coherent, and incoherent interference," *Appl. Opt.* **41**(19), 3978 (2002).
136. S. Franzen, "Surface plasmon polaritons and screened plasma absorption in indium tin oxide compared to silver and gold," *J. Phys. Chem. C* **112**(15), 6027–6032 (2008).
137. H. A. Atwater and A. Polman, "Plasmonics for improved photovoltaic devices," *Nat. Mater.* **9**(3), 205–213 (2010).
138. D. Derkacs et al., "Improved performance of amorphous silicon solar cells via scattering from surface plasmon polaritons in nearby metallic nanoparticles," *Appl. Phys. Lett.* **89**(9), 093103 (2006).
139. B. A. Slovick et al., "Directional control of infrared antenna-coupled tunnel diodes," *Opt. Express* **18**(20), 20960 (2010).
140. K. Chang, X.-D. Wu, and K. Tilley, "Coplanar waveguide fed coplanar strip dipole antenna," *Electron. Lett.* **30**(3), 176–177 (1994).
141. M. Mubarak et al., "Nano-antenna coupled infrared detector design," *Sensors* **18**(11), 3714 (2018).
142. D. M. Benton, "Low-cost detection of lasers," *Opt. Eng.* **56**(11), 114104 (2017).

143. S. Mohammadnejad and M. Aasi, "Laser warning system front-end circuit designing with ambient light cancellation (in press)," in *Int. Conf. Sci. Eng. Manage. Inf. Technol.*, Ankara Yildirim Beyazit University, Turkey (2023).
144. E. Jan, *Low Noise Transimpedance Amplier Design Using Berkeley Analog Generator*, University of California, Berkeley (2020).
145. D. J. A. Groeneveld, *Bandwidth Extension and Noise Cancelling for TIAs*, Mathematics & Computer Science University of Twente (2010).
146. HoomanHashemi, "Transimpedance amplifiers (TIA): choosing the best amplifier for the job," (2017).
147. N. E. Gloire et al., "New development design of low current measurement with noise reduction for high-resolution system," *Am. J. Eng. Appl. Sci.* **11**(2), 756–765 (2018).
148. M. B. Gray et al., "Photodetector designs for low-noise, broadband, and high-power applications," *Rev. Sci. Instrum.* **69**(11), 3755–3762 (1998).
149. J. H. Chuah and D. Holburn, "Design of low-noise high-gain CMOS transimpedance amplifier for intelligent sensing of secondary electrons," *IEEE Sens. J.* **15**(10), 5997–6004 (2015).
150. Electro Optic Components, "SAPLAR 4C-22L-6R-12G datasheet," http://www.electro-optic.ro/saplar4_12_en.html (2023).
151. NERO Industry, "LW100 datasheet," https://neroindustry.com/products/military-laser-warning-system-lw1000/ (2023).
152. HENSOLDT, "ATLAS-2Q datasheet," https://www.hensoldt.net/products/optronics/altas-advanced-laser-threat-alerting-system/ (2023).
153. "Optronics LWS datasheet," https://www.thalesgroup.com/en/worldwide/defence/land-survivability-laser-warning-detector-lwd (2023).
154. ISTEC Services Limited, "Technical specification," https://www.istec.co.uk/product/laser-warning-system-lws/ (2023).
155. P. P. Webb et al., "Improved miniaturized HARLID for laser warning systems having high angular resolution," *Proc. SPIE* **4369**, 194 (2001).

Shahram Mohammadnejad received his BSc degree in electrical engineering from the University of Houston, Houston, Texas, USA, in 1981 and his MSc and PhD degrees in semiconductor material growth and lasers from Shizuoka University, Shizuoka, Japan, in 1990 and 1993, respectively. His research interests include semiconductor material growth, quantum electronics, and semiconductor devices. He is a scientific committee member of the Iranian Conference of Electrical Engineering (ICEE) and Photonics. He is an active professor at IUST and has directed the NRC at IUST.

Meysam Aasi received his BSc degree in electronic engineering from Shahid Shamsipour University of Technical and Vocational, Tehran, Iran, in 2013, and his MSc degree in terahertz detectors based on heavily doped plasmonic semiconductors from Tabriz University, Tabriz, Iran, in 2016. His research interests include infrared lasers, photodetectors, image sensors, laser warning systems, and interferometers. As a PhD candidate, he oversees the NRC and guides several MSc students in completing theses and writing articles.